Comput. Methods Appl. Mech. Engrg. 271 (2014) 296–320

Contents lists available at ScienceDirect

Comput. Methods Appl. Mech. Engrg.

journal homepage: www.elsevier.com/locate/cma

Applying Nagata patches to smooth discretized surfaces used in 3D frictional contact problems

D.M. Neto [a,*], M.C. Oliveira [a], L.F. Menezes [a], J.L. Alves [b]

[a] CEMUC, Department of Mechanical Engineering, University of Coimbra, Polo II, Rua Luís Reis Santos, Pinhal de Marrocos, 3030-788 Coimbra, Portugal
[b] CT2M, Department of Mechanical Engineering, University of Minho, Campus de Azurém, 4800-058 Guimarães, Portugal

ARTICLE INFO

Article history:
Received 14 June 2013
Received in revised form 25 September 2013
Accepted 17 December 2013
Available online 31 December 2013

Keywords:
Surface smoothing method
Nagata patch interpolation
Finite element method
Frictional contact problem
Node-to-Segment
DD3IMP in-house FE code

ABSTRACT

The accurate solution of large deformation frictional contact problems using the finite element method is still a challenging task due to the strong nonlinearities involved. This paper presents a smoothing method applicable to 3D contact surfaces discretized with an arbitrary mesh topology. The quadratic Nagata patch interpolation is adopted to define the smooth surface. The resulting contact surface passes through all nodes of the mesh while providing a smooth description, with at least G^1 continuity at the nodes and *quasi*-G^1 continuity between the patches. Thus, the proposed method avoids the non-physical oscillations in the contact force, which are induced by the traditionally used faceted contact surfaces description, when slave nodes slide over several master segments. Moreover, it allows the accurate evaluation of kinematic variables, leading to important improvements in terms of convergence rate within the Newton–Raphson iteration loop. The developed global and local contact search algorithms, designed for contact surfaces described by Nagata patches, are described in detail. Three numerical examples were selected to illustrate the advantages of the proposed smoothing method, including a complex industrial example of sheet metal forming process. The results show the significant improvements attained with the proposed approach, in terms of efficiency, robustness and accuracy, when compared with the traditional faceted contact surfaces description.

1. Introduction

Contact-impact problems involving friction are of crucial practical importance in many engineering applications, being its numerical simulation still one of the most challenging tasks in computational mechanics [1–7]. Some examples of application comprise various metal forming processes, post-buckling analysis, automobile crashworthiness, biomechanics, among others. Frictional contact problems are difficult to formulate and even more difficult to solve, since they present both geometric and material discontinuity at the contact interface. Hence, the main difficulty lies in dealing with the supplementary conditions for contact and friction, which are inherently non-linear (but also non-smooth), involving variational inequalities and constrained minimizations [3,4,8–12].

In the Finite Element Method (FEM) framework, the most popular approaches used to incorporate the contact constraints in the variational formulation of the initial minimization equilibrium problem are based on: (i) the penalty method [1,2,13]; (ii) the Lagrange multiplier method [14], and (iii) the augmented Lagrange method [3,8,12,15]. The penalty method is the most widely used, due to its simplicity, clear physical meaning and easy numerical implementation. However, the contact

* Corresponding author. Tel.: +351 239790700, fax: +351 239790701.
E-mail addresses: diogo.neto@dem.uc.pt (D.M. Neto), marta.oliveira@dem.uc.pt (M.C. Oliveira), luis.menezes@dem.uc.pt (L.F. Menezes), jlalves@dem.uminho.pt (J.L. Alves).

0045-7825/$ - see front matter © 2014 Published by Elsevier B.V.
http://dx.doi.org/10.1016/j.cma.2013.12.008

constraints are satisfied exactly only for an infinite value of the penalty parameter. On the other hand, the Lagrange multiplier method exactly enforces the non-penetration conditions. Nevertheless it requires additional variables to define the contact reaction forces, which may lead to significant increase of the computational time. A combination of the penalty and the Lagrangian multiplier techniques leads to the so called augmented Lagrangian methods, which takes advantages of both approaches, i.e. the constraints are satisfied exactly for finite values of the penalty parameter and the number of equations to be solved does not increase [16,17].

The strong nonlinearities involved in contact problems are associated with the above mentioned inequality constraints, the non-smooth behavior of the friction law, and the curved geometry of the contacting surfaces [18]. Regarding the last issue, the most widely used contact surface discretization scheme is the Node-to-Segment (NTS) approach, which enforces contact boundary conditions at the finite element nodes using the master–slave formulation [1,2,10,19]. In recent years the Segment-to-Segment (STS) approach associated with the mortar method has also been successfully applied to solve large deformation sliding contact problems [20–23]. Regardless of the approach adopted, the discretization of the contact surfaces is typically achieved using the exterior surface of solid elements, i.e. 2D finite element meshes. Since the faceted geometry represented by lower order elements is not smooth, the surface normal changes suddenly between adjacent facets. Thus, combining a NTS approach with the faceted surface description leads to non-physical jumps in the contact forces, when slave nodes slide over adjacent facet elements, due to the discontinuity of the surface normal field. Some strategies have been suggested to alleviate this problem, which are based on the use of the facets for the shape description while the normal vector field is defined by the interpolation of normal vectors at the nodes [24]. Nevertheless, the faceted description can cause serious numerical instabilities and errors in the predicted forces, as well as, loss of the quadratic convergence rate within a Newton–Raphson scheme, particularly in large deformation finite element analysis involving important relative sliding over high curvature contact surfaces. In order to avoid the problems related with non-smooth contact surface discretization, various surface smoothing algorithms have been proposed in the context of NTS implementations [17,18,25–27]. Most of them use the coordinates of the master nodes to create a smooth curve/surface over the 1D or 2D linear finite element mesh, improving the accuracy of both the gap function and the surface normal vector evaluations. For the particular case of 2D contact problems, Spline and Hermite functions have typically been used to interpolate the mesh nodes in order to attaining at least C^1 continuity in the resulting smooth master surface [25,28–30]. Furthermore, the method proposed by Stadler et al. [27] allows attaining an arbitrary level of continuity in the surfaces by means of employing Non-Uniform Rational B-Spline (NURBS) in the smoothing procedure. However, the desired extension of such interpolation methods to 3D contact problems, involving surfaces with arbitrary mesh topology, cannot be achieved in a straightforward manner since they are usually restricted to structured quadrilateral meshes [12]. Therefore, only a few methods designed for unstructured meshes are available, such as the one proposed by Puso and Laursen [18] that uses Gregory patches, attaining G^1 continuity in the surface representation. Other approach described in [26] uses quartic triangular Bézier patches in the surface description, achieving *quasi*-C^1 continuity surfaces. The subdivision surfaces scheme suggested by Stadler and Holzapfel [31] should also be referenced as an adequate smoothing method for both quadrilateral and triangular unstructured meshes. However, all these methods require special treatment of the nodes where the mesh is unstructured. Furthermore, since the definition of the smoothed contact surfaces and the evaluation of its geometric quantities is typically more difficult, the computational time required to complete the numerical analysis can be higher with the smoothing method than its non-smoothed counterpart [18,26].

In the finite element analysis of sheet metal forming processes, the contact treatment between the sheet and the tools is a very importance issue [24,32,33]. Since the forming tools are usually considered as perfectly rigid, only their exterior surfaces are described in the numerical model. Thus, this is a particular case of the frictional contact problem, since contact is established between a deformable body (metal sheet) and the rigid tools. Hence, continuous analytical surface profiles and various parametric surface descriptions, usually adopted in Computer-Aided Design (CAD), have been used to describe smoothly the exterior tool surfaces, resulting in significant improvements in the solution accuracy when compared with the faceted description [12,32,34,35]. While the application of analytical functions is limited to describe simple geometries, the parameterizations commonly used in CAD are more flexible to describe any arbitrary geometry. Nevertheless, they are characterized by high order interpolation, which leads to high computational cost in the contact treatment [18,36]. Besides, most of the surface models generated by CAD systems are composed by trimmed NURBS patches, which often include many ambiguities such as gaps and overlaps. These geometrical defects restrict the direct application of CAD models in the numerical simulation, requiring a manual treatment of the model before its use in the simulation. This is the main reason why the faceted finite element mesh is still the contact surface description method widely used in FEM codes.

The purpose of this study is to develop a general 3D contact surface smoothing method, adopting the Nagata patch interpolation developed by Nagata [37] and recently improved in [38] to accurately describe 3D discretized curved surfaces. The main concept of the Nagata patch is a quadratic interpolation using only the position and surface normal vectors at the nodes of the mesh. Despite its low order interpolation, the original surface geometry is recovered with good accuracy and the resulting contact surface passes exactly through the nodes of the mesh. The principal advantage of the proposed smoothing method, over the existing ones, is its ability to deal easily with mixed meshes of arbitrary topology, i.e. unstructured surface meshes composed of both triangular and quadrilateral elements. In fact, these meshes are more suitable to deal with complex surface geometries, being the ones commonly adopted in the automatic mesh generation algorithms. Hence, typically the application of FEM in industrial sheet metal forming examples resorts to automatic mesh generation algorithms in the

description of the tool contact surfaces. The proposed smoothing method can be easily extended to smooth discretized deformable body surfaces since the interpolation adopted is simple and completely local [37].

The Nagata patch smoothing method was implemented in DD3IMP in-house finite element code, which has been specifically developed and optimized to simulate sheet metal forming processes [39,40]. The evolution of the deformation process is described by an updated Lagrangian scheme. An explicit approach is used to calculate an approximated first solution for the nodal displacements, the stress states and frictional contact forces in each time increment. Then, the $r_{\min}$ strategy [41,42] is employed to restrict the increment size in order to improve the convergence rate of the iterative Newton–Raphson algorithm, used to correct the first trial solution until the equilibrium state is achieved [39]. The contact with friction is described by the Coulomb law and treated using the augmented Lagrangian approach proposed by Alart and Curnier [8], being the rigid tools originally modeled with Bézier patches. The main characteristic of DD3IMP code is the use of a fully implicit algorithm of Newton–Raphson type to solve, within a single iterative loop, the nonlinearities related with both the mechanical behavior and the contact with friction. The Direct Sparse Solver (DSS) from Intel® Math Kernel Library (Intel® MKL) is employed to solve the non-symmetric large sparse systems of linear equations that arise in this iterative procedure, being this library highly optimized for scientific and engineering applications that require maximum performance. Additionally, some high performance computing techniques have been incorporated to take advantage of multi-core processors, introducing OpenMP directives in the most time consuming branches of the main algorithm [43].

The paper is organized as follows. The formulation of the frictional contact problem is provided in Section 2, being the enforcement of the contact constraints achieved using an augmented Lagrangian approach. In Section 3 the NTS discretization approach is combined with the Nagata patch interpolation method, in order to accomplish the contact treatment between the deformable body and the rigid surfaces in the numerical analysis of frictional contact problems. Special attention is devoted to the algorithm used to accurately describe curved contact surfaces with Nagata patches, based on the linear finite element mesh. Furthermore, the global and local contact search algorithms developed to deal with the particular features of the Nagata patches are discussed. Section 4 presents three numerical examples with distinct levels of complexity, which are used to highlight the advantages of the proposed surface smoothing method. Finally, the principal conclusions of this study are presented in Section 5.

2. Frictional contact problem

This section is devoted to the formulation of the frictional contact problem in the continuum setting, following the rigorous treatment adopted for the problem of contact between deformable bodies presented in [4,12,16]. The formulation involves two fundamental conditions on the common interface between the bodies: the principle of impenetrability and the friction law. These conditions are mathematical described through the normal and frictional contact constraints, which are imposed on the contacting body surfaces.

The 3D frictional contact problem involving the motion of two bodies with large deformation and large sliding is shown in Fig. 1. The pair of deformable bodies $\mathrm{B}^{(\alpha)},\ (\alpha = 1,\ 2)$ in the reference configuration (at time $t = 0$) is represented by the open sets $\Omega_0^{(\alpha)} \subset \Re^3$, while in the deformed configurations ($t \in \Im$ being $\Im$ the time interval of the loading process) is denoted by $\Omega^{(\alpha)} \subset \Re^3$. The deformation mappings of the bodies at instant t are denoted by the differentiable and invertible function $\boldsymbol{\varphi}_t^{(1)}$ and $\boldsymbol{\varphi}_t^{(2)}$, for the bodies $\mathrm{B}^{(1)}$ and $\mathrm{B}^{(2)}$, respectively. For each body, the closure of the open set $\Omega_0^{(\alpha)}$ is denoted as $\bar{\Omega}_0^{(\alpha)}$, being the union of the open set with its boundary $\partial\Omega_0^{(\alpha)} = \Gamma^{(\alpha)}$. The boundary surface $\Gamma^{(\alpha)}$ of each body $\mathrm{B}^{(\alpha)}$ is divided into three non-overlapping parts: $\Gamma_u^{(\alpha)}$ is the region where the displacements are prescribed; $\Gamma_\sigma^{(\alpha)}$ is the region where the tractions are prescribed; and $\Gamma_c^{(\alpha)}$ is the region where contact constraints will be defined due to the potential frictional contact between the bodies (cf. Fig. 1). The spatial counterparts of the three disjoint parts are obtained with the corresponding mapping functions, being denoted by $\gamma_u^{(\alpha)}$, $\gamma_\sigma^{(\alpha)}$ and $\gamma_c^{(\alpha)}$, respectively. Moreover, the partition in three surface sets must satisfy the following conditions:

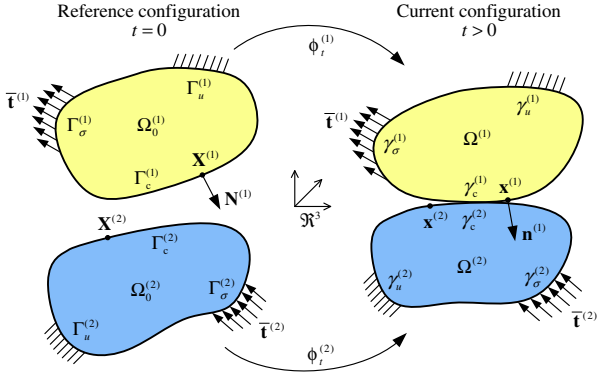

Fig. 1. Notation used in the definition of the contact problem between two deformable bodies involving large deformations.

$$\Gamma_u^{(\alpha)} \cup \Gamma_\sigma^{(\alpha)} \cup \Gamma_c^{(\alpha)} = \Gamma^{(\alpha)} = \partial\Omega^{(\alpha)} \tag{1}$$

and

$$\Gamma_u^{(\alpha)} \cap \Gamma_\sigma^{(\alpha)} = \Gamma_\sigma^{(\alpha)} \cap \Gamma_c^{(\alpha)} = \Gamma_u^{(\alpha)} \cap \Gamma_c^{(\alpha)} = \varnothing\,. \tag{2}$$

The spatial coordinates of a generic material point in the reference configuration are denoted by $\mathbf{X}^{(\alpha)}$, while the position vector of its counterpart in the deformed configuration at time t is represented by $\mathbf{x}^{(\alpha)} = \boldsymbol{\varphi}_t^{(\alpha)}(\mathbf{X}^{(\alpha)})$, as shown in Fig. 1. Therefore, the position vector of all material points of the body $B^{(\alpha)}$ in the current configuration can be defined as $\mathbf{x}^{(\alpha)} = \mathbf{X}^{(\alpha)} + \mathbf{u}^{(\alpha)}$, where $\mathbf{u}^{(\alpha)}$ is the displacement field associated with a given point at the instant $t \in \mathfrak{I}$.

Assuming *quasi*-static response (no inertia terms) within large deformation framework, the strong form of the linear momentum balance and the prescribed boundary conditions for each body $B^{(\alpha)}$, with respect to the reference configuration, are governed by the following equations:

$$\begin{cases} \mathrm{Div}\,\mathbf{P}^{(\alpha)} + \mathbf{f}^{(\alpha)} = \mathbf{0} & \text{in } \Omega_0^{(\alpha)}, \\ \mathbf{P}^{(\alpha)}\mathbf{N}^{(\alpha)} = \bar{\mathbf{t}}^{(\alpha)} & \text{on } \Gamma_\sigma^{(\alpha)}, \\ \mathbf{u}^{(\alpha)} = \bar{\mathbf{u}}^{(\alpha)} & \text{on } \Gamma_u^{(\alpha)}, \end{cases} \tag{3}$$

where $\mathbf{P}^{(\alpha)}$ is the first Piola–Kirchhoff stress tensor, $\mathbf{f}^{(\alpha)} : \Omega_0^{(\alpha)} \times \mathfrak{I} \to \Re^3$ denote the prescribed volume forces applied on the reference configuration and $\mathbf{N}^{(\alpha)}$ is the outward unit normal vector of the boundary $\Gamma^{(\alpha)}$ in the reference configuration. The prescribed tractions and displacements on the body boundary are denoted by $\bar{\mathbf{t}}^{(\alpha)} : \Gamma_\sigma^{(\alpha)} \times \mathfrak{I} \to \Re^3$ and $\bar{\mathbf{u}}^{(\alpha)} : \Gamma_u^{(\alpha)} \times \mathfrak{I} \to \Re^3$, respectively.

2.1. Normal and frictional contact conditions

In the subsequent analysis the bodies $B^{(1)}$ and $B^{(2)}$ are referred as the slave and master body, respectively. Thus, the contact surface $\Gamma_c^{(1)}$ is chosen as the slave surface and the surface $\Gamma_c^{(2)}$ is chosen as the master one. In order to take into account the mechanical interactions between the bodies, each material point $\mathbf{x}^{(1)}$ of the slave surface requires the identification of its counterpart point on the master surface $\gamma_c^{(2)}$. This correspondence is defined by means of the closest point projection of $\mathbf{x}^{(1)}$ on the surface $\gamma_c^{(2)}$, carried out in the current configuration, for each instant $t \in \mathfrak{I}$. Assuming that the solution achieved with the projection method is unique (master surface at least locally convex), the position vector of the point on the master surface that minimizes the distance to the point $\mathbf{x}^{(1)}$ is obtained through the normal distance function d_+^{n} (always positive), defined as:

$$d_+^{\mathrm{n}}(\mathbf{x}^{(1)}) = \arg \min_{\mathbf{x}^{(2)} \in \gamma_c^{(2)}} |\mathbf{x}^{(1)} - \mathbf{x}^{(2)}(\xi^1, \xi^2)|, \tag{4}$$

where $\boldsymbol{\xi} = (\xi^1, \xi^2)$ are the convective coordinates resulting from the parameterization of the master surface. The minimal distance problem presented in Eq. (4) corresponds to the orthogonal projection of the slave point $\mathbf{x}^{(1)}$ onto the master surface $\gamma_c^{(2)}$, as shown in Fig. 2. The resulting projection point and other quantities evaluated at the solution point are denoted by a bar over the quantity, such that the position vector is denoted by $\bar{\mathbf{x}}^{(2)} = \mathbf{x}^{(2)}(\bar{\xi}^1, \bar{\xi}^2)$. Hence, the signed normal distance function (also called gap function) can be expressed as the signed distance between the points $\mathbf{x}^{(1)}$ and $\bar{\mathbf{x}}^{(2)}$, measured in the normal direction to the master surface, given by:

$$d^{\mathrm{n}}(\mathbf{x}^{(1)}) = (\mathbf{x}^{(1)} - \bar{\mathbf{x}}^{(2)}) \cdot \bar{\mathbf{n}}^{(2)}\,, \tag{5}$$

with $\bar{\mathbf{n}}^{(2)}$ denoting the outward unit normal to the master surface $\gamma_c^{(2)}$, at material point $\bar{\mathbf{x}}^{(2)}$. Applying this definition, the signed normal distance d^{n} is positive if the contact is open and negative when penetration of the bodies takes place [7,8].

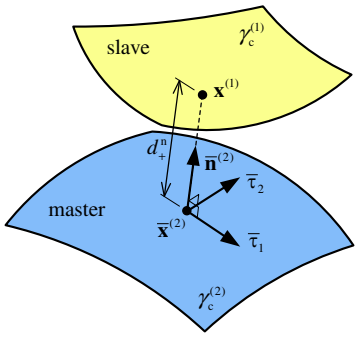

Fig. 2. Definition of the orthogonal projection of the slave point $\mathbf{x}^{(1)}$ onto the master surface and the normal distance function d_+^{n}.

The second kinematic variable to be defined is the tangential slip velocity $\dot{\boldsymbol{\delta}}^{\mathrm{t}}$, which is related to the time evolution of the solution point $(\bar{\xi}^1,\ \bar{\xi}^2)$ defined by the minimal distance problem. Assuming the starting condition $\dot{d}^{\mathrm{n}} = 0$ [44,45], the tangential slip velocity, which is the difference between the velocities of contacting points $\mathbf{x}^{(1)}$ and $\bar{\mathbf{x}}^{(2)}$ (slip rate of $\mathbf{x}^{(1)}$ relative to the adjacent surface $\gamma_{\mathrm{c}}^{(2)}$), is given as follows:

$$\dot{\boldsymbol{\delta}}^{\mathrm{t}} = \dot{\mathbf{x}}^{(1)} - \dot{\bar{\mathbf{x}}}^{(2)} = \dot{\bar{\xi}}^{\beta}\bar{\boldsymbol{\tau}}_{\beta}, \tag{6}$$

where $\boldsymbol{\tau}_{\beta}$ denotes the covariant basis vectors on the parameterized master surface (physically defines tangent vectors), which are indicated in Fig. 2 for the particular solution point $\bar{\mathbf{x}}^{(2)}$.

Since the contact formulation considers that all geometric quantities are evaluated on the master surface, the contact traction developed on the master surface is denoted by $\mathbf{t}_{\mathrm{c}} := \mathbf{t}_{\mathrm{c}}^{(2)} = -\mathbf{t}_{\mathrm{c}}^{(1)}$, which can be decomposed into a normal and tangential components:

$$\mathbf{t}_{\mathrm{c}} = \mathbf{t}_{\mathrm{c}}^{\mathrm{n}} + \mathbf{t}_{\mathrm{c}}^{\mathrm{t}} = t_{\mathrm{c}}^{\mathrm{n}}\mathbf{n} + t_{\mathrm{c}_{\alpha}}^{\mathrm{t}}\boldsymbol{\tau}_{\alpha}, \tag{7}$$

where $\mathbf{n} := \bar{\mathbf{n}}^{(2)}$ stands for the current unit normal vector of the master surface $\gamma_{\mathrm{c}}^{(2)}$ in $\bar{\mathbf{x}}^{(2)}$. The amplitude of the normal component of the contact traction denoted by $t_{\mathrm{c}}^{\mathrm{n}} = \mathbf{t}_{\mathrm{c}} \cdot \mathbf{n}$ is exerted in the surface normal direction, while the tangential component $\mathbf{t}_{\mathrm{c}}^{\mathrm{t}}$ acts in the plane tangent to the contact surface at the material point $\mathbf{x}^{(1)}$, as schematically presented in Fig. 3.

The normal contact constraint, expressed by the unilateral contact law, postulates the non-penetration constraint condition between the bodies. Typically the unilateral contact law is formulated with the aid of the following three relationships, known as the Karush–Kuhn–Tucker conditions [46]:

$$\begin{aligned} &d^{\mathrm{n}} \geqslant 0, \\ &t_{\mathrm{c}}^{\mathrm{n}} \leqslant 0, \\ &t_{\mathrm{c}}^{\mathrm{n}} d^{\mathrm{n}} = 0, \end{aligned} \tag{8}$$

where the first condition states that no penetration may occur between the bodies and the second one imposes that contact normal traction is compressive. The third condition expresses a mechanical complementarity condition, imposing that d^{n} and $t_{\mathrm{c}}^{\mathrm{n}}$ cannot be simultaneously non-null. These three conditions characterize the relationship between the contact variables d^{n} and $t_{\mathrm{c}}^{\mathrm{n}}$, which is graphically represented in Fig. 4(a), where the contact conditions are distinguished: gap and contact.

The classical Coulomb friction law is one of the most widely used [1,3,8], being also adopted in this work. The tangential contact constraint dictated by the friction law is defined in terms of the tangential slip velocity $\dot{\boldsymbol{\delta}}^{\mathrm{t}}$ and the tangential component of contact traction $\mathbf{t}_{\mathrm{c}}^{\mathrm{t}}$ (frictional force), with the normal component $t_{\mathrm{c}}^{\mathrm{n}}$ as a parameter [12]. Hence, the constraints imposed to the frictional force, both in terms of amplitude and direction, are formulated through the following three conditions:

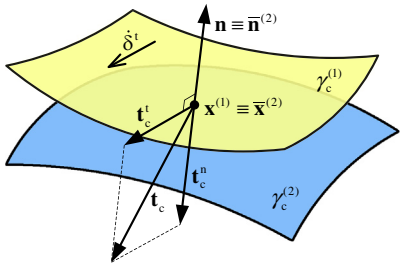

Fig. 3. Decomposition of the contact force $\mathbf{t}_{\mathrm{c}}$ into normal and tangential components.

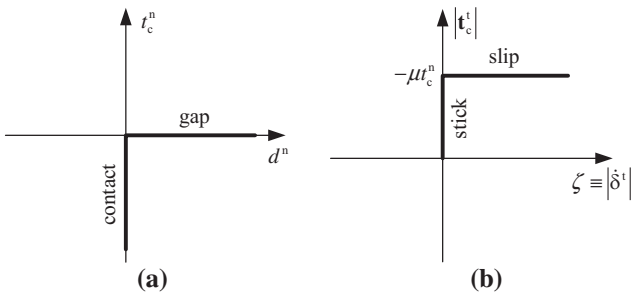

Fig. 4. Relationships between kinematic and static variables dictated by the contact constraints: (a) unilateral contact law; (b) Coulomb friction law.

$$\begin{aligned} &\dot{\boldsymbol{\delta}}^{\mathrm{t}} - \zeta \frac{\mathbf{t}_{\mathrm{c}}^{\mathrm{t}}}{|\mathbf{t}_{\mathrm{c}}^{\mathrm{t}}|} = \mathbf{0} \quad \text{with } \zeta \geqslant 0, \\ &\phi := |\mathbf{t}_{\mathrm{c}}^{\mathrm{t}}| + \mu t_{\mathrm{c}}^{\mathrm{n}} \leqslant 0, \\ &\phi\zeta = 0, \end{aligned} \tag{9}$$

where μ is the friction coefficient and ζ is the slip factor, being these conditions usually denominated as slip rule, friction law and complementary condition, respectively. The slip rule dictates that the frictional force acting on the master body $\mathbf{t}_{\mathrm{c}}^{\mathrm{t}}$ arises in the same direction than the tangential slip velocity $\dot{\boldsymbol{\delta}}^{\mathrm{t}}$ of the slave point $\mathbf{x}^{(1)}$, as presented in Fig. 3. The condition presented in Eq. $(11)_2$ represents the Coulomb friction law, which establishes the maximum magnitude for the frictional force [44]. The complementary condition shown in Eq. $(11)_3$ imposes that when the frictional force is less than the Coulomb limit ($\phi < 0$), the tangential slip velocity must be zero, which corresponds to $\zeta = 0$. This is called the stick contact state since no sliding occurs between the bodies. When the friction force attains the Coulomb limit ($\phi = 0$), the sliding between the bodies is allowed $\zeta > 0$ and therefore it is called slip contact state. Fig. 4(b) presents the Coulomb friction law with the distinction between the contact statuses: stick and slip.

2.2. Augmented Lagrangian method

In most of engineering applications it is acceptable to consider that the contact occurs between a deformable body and curved rigid surfaces. In the following, the attention is restricted to the frictional contact problem between a deformable body and a smooth rigid obstacle. Consequently, all numerical calculations are restricted to only one body, being the surface of the second one used to impose the frictional contact constraints.

An extension of the augmented Lagrangian approach proposed in [8,34] is used in this study for treating the contact and friction inequality constraints. This method involves a mixed formulation where the kinematic and contact static variables are the final unknowns of the problem. The contact constraints are transferred from the primal variables $\mathbf{v}$ to the dual variables λ^{n} and $\boldsymbol{\lambda}^{\mathrm{t}}$, which can be physically identified as the normal and tangential components of the contact traction, respectively. The generalized Newton method is employed to solve the resulting mixed system of non-linear and partially non-differentiable equations [6,8,39,47]. Following Alart and Curnier [8], the *quasi*-augmented Lagrangian function is defined as follows:

$$L(\mathbf{v},\boldsymbol{\lambda}) = \boldsymbol{\Phi}(\mathbf{v}) + d^{\mathrm{n}}\lambda^{\mathrm{n}} + \boldsymbol{\delta}^{\mathrm{t}}\cdot\boldsymbol{\lambda}^{\mathrm{t}} + \frac{r}{2}|d^{\mathrm{n}}|^2 - \frac{1}{2r}\mathrm{dist}^2(\lambda^{\mathrm{n}} + rd^{\mathrm{n}},\ \Re^{-}) + \frac{r}{2}|\boldsymbol{\delta}^{\mathrm{t}}|^2 - \frac{1}{2r}\mathrm{dist}^2(\boldsymbol{\lambda}^{\mathrm{t}} + r\boldsymbol{\delta}^{\mathrm{t}},\ C^{\mathrm{aug}}), \tag{10}$$

where $\boldsymbol{\Phi}$ is the differentiable strain energy potential that characterizes the material response of the body under analysis and r is a positive penalty parameter. The operator $\mathrm{dist}(x, C)$ denotes the distance from x to C, being the augmented convex disk defined as $C^{\mathrm{aug}}(t_{\mathrm{c}}^{\mathrm{n}} + rd^{\mathrm{n}}) = C(\mathrm{proj}_{\Re^-}(t_{\mathrm{c}}^{\mathrm{n}} + rd^{\mathrm{n}}))$, with $\mathrm{proj}_{\Re^-}(x)$ denoting the projection of x on $\Re^-$. In *quasi*-static analysis, the slip rate $\dot{\boldsymbol{\delta}}^{\mathrm{t}}$ can be approximated by the slip displacement increment $\boldsymbol{\delta}^{\mathrm{t}} = \Delta t\,\dot{\boldsymbol{\delta}}^{\mathrm{t}}$. Since the augmented Lagrangian function $L(\mathbf{v},\boldsymbol{\lambda})$ is C^1-differentiable with respect to $\mathbf{v}$ and $\boldsymbol{\lambda}$, the saddle-point $(\mathbf{u},\ \mathbf{t}_{\mathrm{c}})$ corresponds to the solution of the original constrained optimization problem [8,12,48]. Hence, the equilibrium of the deformable body in frictional contact with a rigid obstacle is governed by the following non-linear system of equations:

$$\begin{cases} \mathbf{F}^{\mathrm{int}}(\mathbf{u}) - \mathbf{F}^{\mathrm{ext}} + \mathbf{F}^{\mathrm{c}}(\mathbf{u},\mathbf{t}_{\mathrm{c}}) = \mathbf{0}, \\ -\frac{1}{r}(\mathbf{t}_{\mathrm{c}} - \mathbf{F}^{\mathrm{c}}(\mathbf{u},\mathbf{t}_{\mathrm{c}})) = \mathbf{0}, \end{cases} \tag{11}$$

where $\mathbf{F}^{\mathrm{int}}$ is the internal force vector and $\mathbf{F}^{\mathrm{ext}}$ the external one, which is assumed to be independent of the displacement field $\mathbf{u}$. The continuous frictional contact operator $\mathbf{F}^{\mathrm{c}}(\mathbf{u},\boldsymbol{\lambda})$ for a slave point is defined as follows:

$$\mathbf{F}^{\mathrm{c}}(\mathbf{v},\boldsymbol{\lambda}) = \mathrm{proj}_{\Re^-}(\sigma^{\mathrm{n}})\mathbf{n} + \mathrm{proj}_{C^{\mathrm{aug}}}(\boldsymbol{\sigma}^{\mathrm{t}}), \tag{12}$$

with the augmented Lagrange multipliers defined as $\sigma^{\mathrm{n}} = \lambda^{\mathrm{n}} + rd^{\mathrm{n}}$ and $\boldsymbol{\sigma}^{\mathrm{t}} = \boldsymbol{\lambda}^{\mathrm{t}} + r\boldsymbol{\delta}^{\mathrm{t}}$. The continuity of the contact with friction operator $\mathbf{F}^{\mathrm{c}}$ allows evaluating the Jacobian matrix required to solve the system of equations with a generalized Newton method. The frictional contact operators proposed by Heege and Alart [34] for the generalized case of strongly curved contact surfaces are adopted in this study.

3. Finite element discretization

This section deals with the application of the FEM to the discretization of the continuum frictional contact problem presented in Section 2. Among the different discretization techniques for large slip contact problems, the Node-to-Segment (NTS) algorithm is the most widely used due to its simplicity, physical meaning and flexibility [1,6,10,14,19]. In this work the deformable body is discretized by means of low order solid finite elements using the traditional finite element method [49]. Moreover, the curved surface of the involved rigid bodies is discretized with smooth parametric patches, contrasting with the traditional faceted finite element description adopted in the generality of commercial FEM codes. Therefore, in the contest of the NTS formulation, the slave surface is represented by single nodes resulting from the finite element discretization of the slave body, while the master surface is approximated by a group of smooth patches. The impenetrability and

friction law conditions (Eqs. (8) and (9), respectively) are enforced such that the slave nodes must not penetrate their opposing master segments (facets or patches) neither violate the Coulomb friction law.

When the finite element mesh is adopted in the description of the master surface, the contact kinematic quantities d^n and ξ^β are evaluated in terms of the current position of the slave nodes relative to the faceted approximation of the master surface. Since the surface normal vector is used in the definition of both the signed normal distance, presented in Eq. (5), and contact traction presented in Eq. (7), its discontinuity across neighbor elements typically leads to non-physical jumps in the solution as well as convergence problems [30]. The application of a smooth description for the master surface avoids the occurrence of these problems during the enforcement of the contact conditions [18,30]. Concerning the particular case of the contact between a deformable body and rigid curved obstacles, various smoothing procedures have been proposed in the context of NTS formulation [18,25–31]. In the framework of NTS smoothing formulations, each slave node interacts with a smooth master surface presenting a high level of continuity. Therefore, several alternatives have been suggested to define C^1 smooth surfaces created on faceted finite element meshes using the coordinates of the master nodes [26,28]. In this work the rigid surfaces of arbitrary shape will be described with Nagata patches. In the following, the nodes of the master surface will be refereed as vertices in order to distinguish them from the nodes of the deformable body.

3.1. Rigid surfaces described by Nagata patches

A new interpolation method developed by Nagata [37], which can be applied to both curves and surfaces, has been recently successfully applied to diverse engineering problems [24,50,51]. The idea behind the Nagata patch interpolation is the simple and local quadratic interpolation using the information concerning the position vector and surface normal vector of the mesh vertices composing the curve/patch. The reduced interpolation degree associated with the completely local support allows evaluating the required contact kinematic variables straightforwardly using a reduced computational cost. Furthermore, the *quasi*-G^1 continuity between Nagata patches produces a smooth contact surface description, which means that the direction of the first derivative (or surface normal vector) in the boundaries between patches tends to be the same. This particular feature avoids non-physical jumps in the contact force when a slave node crosses two neighboring patches [31,52]. The main drawback associated with the currently available smoothing methods is its applicability to 3D unstructured surface meshes [18,31]. In fact, the difficulty to create a smooth surface over the faceted unstructured mesh is overcome with the application of the Nagata patch interpolation since the approach is completely local. Moreover, the formulation can be applied to general n-sided patches, such as triangular and quadrilateral patches (or a mix of both) [37], being this a promising interpolation method to be applied in the computational contact mechanics [24,37,38].

The main idea of the proposed method is to smooth relatively coarse meshes using the Nagata patch interpolation, being the discretized surfaces produced using any mesh generator from the CAD model. However, most of CAD models containing the information regarding the curved rigid surfaces are plagued by geometrical or topological errors and inconsistencies [53]. Therefore, in order to use the model in the mesh generation it is always necessary to perform some geometry repair, clean-up, and preparation. In fact, many errors and inconsistencies (e.g. gaps/overlaps between abutting surfaces) are resulting from the lack of a robust solution to the surface intersection problem [53,54].

The flowchart presented in Fig. 5 shows the proposed procedure to describe the curved contact surfaces with Nagata patches from the information of the CAD model. The procedure can be divided in three steps: mesh generation, vertex

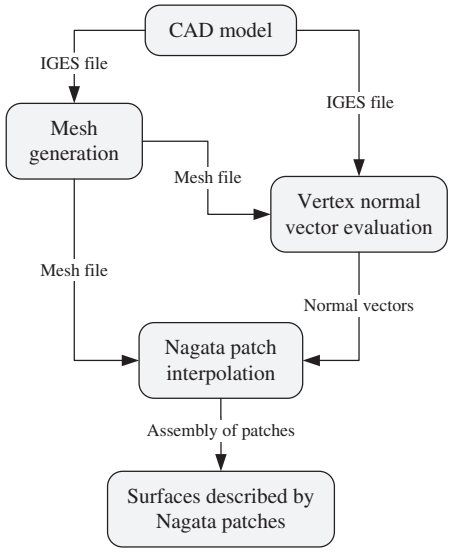

Fig. 5. Procedure followed to describe the contact surfaces from the CAD model information.

normal vector evaluation and Nagata patch interpolation. This interpolation method allows smoothing both structured and unstructured meshes. Indeed, the discretization of the contact surfaces with unstructured meshes is more attractive, both from the user point of view and the consumed time, since the meshes are fast and easily obtained using automatic meshing algorithms. Moreover, due to the way the Nagata patch is created, the models of the discretized contact surfaces can be composed by both triangular and quadrilateral faceted elements. The information contained in the generated mesh file, required to the local interpolation, is the position vector of each mesh vertex and the finite element connectivity (vertices composing each finite element). Since any mesh generator allows exporting mesh files containing all this information, a wide variety of mesh generator packages can be employed. Concerning the evaluation of the surface normal vector in each vertex of the mesh, the strategy applied in this study takes advantage of the CAD model definition together with the mesh file, as shown in Fig. 5. The central idea behind this strategy is to use the IGES file format of the CAD model to project each mesh vertex on the corresponding NURBS surface in order to evaluate the partial derivatives of the surface and subsequently its normal vector. This strategy was developed by the authors and is presented in [55]. The application of this strategy when compared with the one that resorts to weighting adjacent face normal vectors leads to the best accuracy in the Nagata interpolation, evidencing the effect of the normal vector in the interpolation accuracy [38,55,56].

Once the finite element mesh is selected and the surface normal vectors are evaluated (required input parameters), the Nagata patch interpolation can be correctly employed to smooth the surface mesh. Since the interpolation method is completely local, its application to each faceted element can be performed independently (suitable for parallel processing), leading to a model composed by an assembly of patches. The proposed smoothing method applicability is enhanced by the use of neutral CAD formats to evaluate the required surface normal vector in each vertex of the mesh, being the widely used IGES file format the one adopted in this study. Moreover, the possibility to use diverse types of mesh files in the definition of the contact surface, allows creating readily new surface geometries, from diverse mesh generators software packages. Fig. 6 presents an example of a forming tool geometry described by faceted finite elements. The normal vectors evaluated through the approach proposed in [55] are indicated in the discretized surface model and are used in the interpolation adopted to smooth the surface mesh.

3.1.1. Nagata patch interpolation

The formulation of the Nagata patch interpolation is briefly described, highlighting its mathematical simplicity and local support. The main idea is to recover the original surface geometry with good accuracy, by using the position and surface normal vectors in each vertex of the faceted finite element mesh. Starting with a 2D interpolation example applied to an edge, which is defined by its end points with position vectors $\mathbf{x}_0$ and $\mathbf{x}_1$, the Nagata interpolation of the edge is given by the following curve:

$$\mathbf{C}(\xi^1) = \mathbf{x}_0 + (\mathbf{x}_1 - \mathbf{x}_0 - \mathbf{c})\xi^1 + \mathbf{c}(\xi^1)^2, \tag{13}$$

where ξ^1 is the local coordinate of the curve, which satisfy the condition $0 \leqslant \xi^1 \leqslant 1$. The curvature is added to the edge through the parameter $\mathbf{c}$, which is determined from the boundary conditions at edge end points, as follows:

$$\mathbf{c}(\mathbf{x}_0, \mathbf{x}_1, \mathbf{n}_0, \mathbf{n}_1) = \begin{cases} \frac{[\mathbf{n}_0,\ \mathbf{n}_1]}{1-a^2} \begin{bmatrix} 1 & -a \\ -a & 1 \end{bmatrix} \begin{Bmatrix} \mathbf{n}_0 \cdot (\mathbf{x}_1 - \mathbf{x}_0) \\ -\mathbf{n}_1 \cdot (\mathbf{x}_1 - \mathbf{x}_0) \end{Bmatrix} & (a \neq \pm 1), \\ \mathbf{0} & (a = \pm 1), \end{cases} \tag{14}$$

where the unit normal vectors at the end points $\mathbf{x}_0$ and $\mathbf{x}_1$ are denoted by $\mathbf{n}_0$ and $\mathbf{n}_1$, respectively. The cosine of the angle between the normal vectors is expressed by $a = \mathbf{n}_0 \cdot \mathbf{n}_1$ and $[\cdot, \cdot]$ indicates a matrix composed by two vectors. The above interpolation algorithm expressed by Eqs. (13) and (14) is the basis to apply the Nagata interpolation to general n-sided

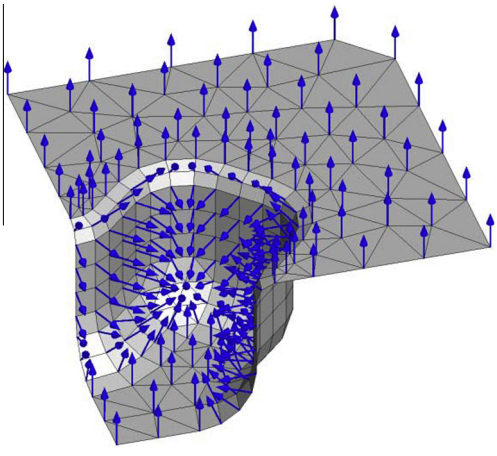

Fig. 6. Forming tool geometry described by faceted finite elements, including surface normal vectors at the vertices.

patches, such as triangular and quadrilateral patches. Firstly, each edge of the faceted finite element is replaced by a Nagata curve given through Eq. (13), and then its interior is filled.

In case of a triangular patch, the Nagata patch interpolated is given by the following quadratic polynomial:

$$\boldsymbol{P}_t(\xi^1,\ \xi^2) = \mathbf{c}_{00} + \mathbf{c}_{10}\xi^1 + \mathbf{c}_{01}\xi^2 + \mathbf{c}_{11}\xi^1\xi^2 + \mathbf{c}_{20}(\xi^1)^2 + \mathbf{c}_{02}(\xi^2)^2, \tag{15}$$

where ξ^1 and ξ^2 are the local coordinates satisfying the patch domain validity expressed by $0 \leqslant \xi^2 \leqslant \xi^1 \leqslant 1$. The six coefficient vectors $\mathbf{c}_{ij}$, whose notation adopted in the patch definition is $\mathbf{c}_{ij}(\xi^1)^i(\xi^2)^j$, are calculated using only the position and surface normal vectors at the mesh vertices, being defined as follows:

$$\begin{aligned}
\mathbf{c}_{00} &= \mathbf{x}_{00},\\
\mathbf{c}_{10} &= \mathbf{x}_{10} - \mathbf{x}_{00} - \mathbf{c}_1,\\
\mathbf{c}_{01} &= \mathbf{x}_{11} - \mathbf{x}_{10} + \mathbf{c}_1 - \mathbf{c}_3,\\
\mathbf{c}_{11} &= \mathbf{c}_3 - \mathbf{c}_1 - \mathbf{c}_2,\\
\mathbf{c}_{20} &= \mathbf{c}_1,\\
\mathbf{c}_{02} &= \mathbf{c}_2,
\end{aligned} \tag{16}$$

where $\mathbf{c}_1$, $\mathbf{c}_2$ and $\mathbf{c}_3$ are the coefficient vectors, defined by Eq. (14), for the edges $(\mathbf{x}_{00}, \mathbf{x}_{10})$, $(\mathbf{x}_{10}, \mathbf{x}_{11})$ and $(\mathbf{x}_{00}, \mathbf{x}_{11})$, respectively. The quadrilateral Nagata patch is obtainable in a similar way as the triangular patch, being defined by:

$$\boldsymbol{P}_q(\xi^1,\ \xi^2) = \mathbf{c}_{00} + \mathbf{c}_{10}\xi^1 + \mathbf{c}_{01}\xi^2 + \mathbf{c}_{11}\xi^1\xi^2 + \mathbf{c}_{20}(\xi^1)^2 + \mathbf{c}_{02}(\xi^2)^2 + \mathbf{c}_{21}(\xi^1)^2\zeta + \mathbf{c}_{12}\xi^1(\xi^2)^2, \tag{17}$$

where the validity patch domain, dictated by the local coordinates, is given by $0 \leq \xi^1,\ \xi^2 \leq 1$. The coefficients $\mathbf{c}_{ij}$ are given by:

$$\begin{aligned}
\mathbf{c}_{00} &= \mathbf{x}_{00},\\
\mathbf{c}_{10} &= \mathbf{x}_{10} - \mathbf{x}_{00} - \mathbf{c}_1,\\
\mathbf{c}_{01} &= \mathbf{x}_{01} - \mathbf{x}_{00} - \mathbf{c}_4,\\
\mathbf{c}_{11} &= \mathbf{x}_{11} - \mathbf{x}_{10} - \mathbf{x}_{01} + \mathbf{x}_{00} + \mathbf{c}_1 - \mathbf{c}_2 - \mathbf{c}_3 + \mathbf{c}_4,\\
\mathbf{c}_{20} &= \mathbf{c}_1,\\
\mathbf{c}_{02} &= \mathbf{c}_4,\\
\mathbf{c}_{21} &= \mathbf{c}_3 - \mathbf{c}_1,\\
\mathbf{c}_{12} &= \mathbf{c}_2 - \mathbf{c}_4,
\end{aligned} \tag{18}$$

where $\mathbf{c}_1$, $\mathbf{c}_2$, $\mathbf{c}_3$ and $\mathbf{c}_4$ are the coefficients defined by Eq. (14) for the edges $(\mathbf{x}_{00}, \mathbf{x}_{10})$, $(\mathbf{x}_{10}, \mathbf{x}_{11})$, $(\mathbf{x}_{01}, \mathbf{x}_{11})$ and $(\mathbf{x}_{00}, \mathbf{x}_{01})$, respectively.

Note that no matrix inversion is required to determine the interpolation coefficients since they are evaluated through Eq. (14) using the position vectors and the normal vectors at the vertices. For more details about the Nagata patch interpolation and the mathematical expressions to evaluate the $\mathbf{c}_{ij}$ coefficients, the reader can refer to [37]. Since the Nagata patch interpolation is characterized by the quadratic degree, the approximation capability is rather limited. Therefore, some improvements to the original formulation were proposed by the authors [38] and by Boschiroli et al. [57] in order to avoid the generation of very sharp surfaces in the description of contact surfaces. The used methodology comprises the modification of Eq. (14) by extending the domain for applying linear interpolation ($\mathbf{c} = \mathbf{0}$), which was originally limited to $a = \pm 1$.

3.1.2. Smoothing method accuracy

This section deals with the influence of the discretization on the resulting smoothed curve/surface accuracy. Both the geometric and the normal vector error distributions obtained when employing Nagata patches in the surface description are compared with the ones resulting from the traditional faceted finite element mesh description. Since constant radius fillet surfaces and surfaces of revolution are frequently employed to create smooth contact surfaces, the circular arc and the sphere are the selected geometries to perform this study. The geometric accuracy of the approximation is evaluated through the radial error δ_r, which is defined by the deviation between the discretized curve/surface (faceted and smoothed) and the analytical geometry. Considering a circular arc of radius r, the radial error associated with its discretization is defined as:

$$\delta_r(\xi^1) = \frac{\tilde{r}(\xi^1) - r}{r} \times 100\%, \tag{19}$$

where $\tilde{r}(\xi^1)$ is the local radius of the approximated circular arc and ξ^1 is the local coordinate of the interpolated curve, as defined in Eq. (13). The radius resulting from the interpolation is not constant in all arc length, even if the normal vectors required by the Nagata interpolation are determined using the analytical function of the circular arc.

The effect of the discretization, both in the piecewise linear interpolation and in the Nagata interpolation method, is studied using the circular arc geometry. Fig. 7 presents the comparison of the maximum norm of the radial error between the piecewise linear interpolation and the quadratic Nagata interpolation, in function of the normalized arc length (ℓ/r). The

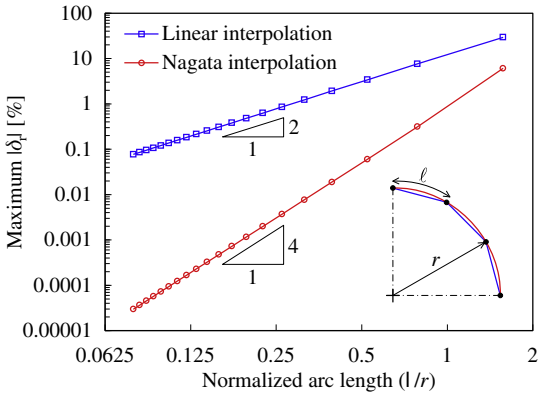

Fig. 7. Comparison of the maximum norm of the radial error between the piecewise linear interpolation and the Nagata interpolation applied to a circular arc.

range considered for the normalized arc length is from 1.571 until 0.157, which corresponds to dividing a quarter of circle from 1 to 10 equal divisions, respectively. Both approximation methods attain its maximum norm of radial error at the midpoint of the curve ($\xi^1 = 0.5$), being the Nagata patch always outside the circle arc while the piecewise linear approximation is always inside the original arc, as exemplified in the scheme of Fig. 7. The application of the Nagata interpolation clearly results in a more accurate representation of the circular arc [38], being quartic the order of convergence in the radial error, while the piecewise linear approximation leads only to quadratic convergence.

The radial error distribution obtained with both approximation methods is also studied using a spherical surface of radius r. The expression presented in Eq. (19) can also be used, but now the local radius becomes a function of the two local coordinates $\check{r}(\xi^1, \xi^2)$. The approximated local radius resultant from the Nagata patch interpolation algorithm is evaluated indirectly through the application of Eq. (15) and/or Eq. (17). Fig. 8(a) and (b) presents a spherical surface discretized by the traditional faceted finite elements and smoothed with Nagata patches, respectively. A quick qualitative error analysis shows that the faceted approximation provides poor accuracy when compared with the smoothed model. The right-hand side of each discretized surface illustrates the quantitative error analysis by means of radial error distribution. The error is negative in the approximated spherical surface when the faceted finite element mesh is employed, either using triangular or quadrilateral finite elements. On the other hand, the application of the Nagata interpolation to smooth the geometry leads to an approximated geometry where the error tends to be positive in the triangular patches and negative in the quadrilateral patches, as shown in Fig. 8(b).

The error in the surface normal vector resulting from the approximation is also evaluated for the spherical surface. This error is directly associated with the geometric continuity of the approximated surface, which is a key point for the robustness of the smoothing method when applied to computational contact mechanics. For the spherical surface, the surface normal vector error is defined as:

$$\delta_n(\xi^1, \xi^2) = \cos^{-1}(\mathbf{n}_{\text{approx}}(\xi^1, \xi^2) \cdot \mathbf{n}_{\text{analy}}) \ [^\circ], \tag{20}$$

where $\mathbf{n}_{\text{approx}}$ is the surface normal vector of the approximated surface, while the normal vector of the analytical sphere is denoted by $\mathbf{n}_{\text{analy}}$. Fig. 9 presents the comparison between the surface normal vector error distributions obtained with faceted elements and Nagata patches. The maximum value of error occurs in the vertices of the faceted finite elements, while

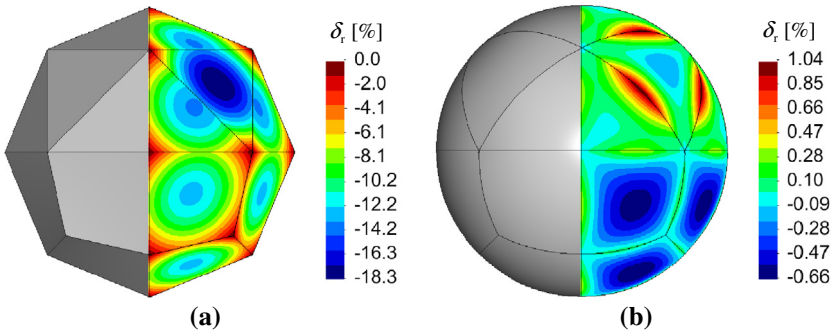

Fig. 8. Radial error distribution resultant from the description of a spherical surface using: (a) faceted finite elements and (b) Nagata patches.

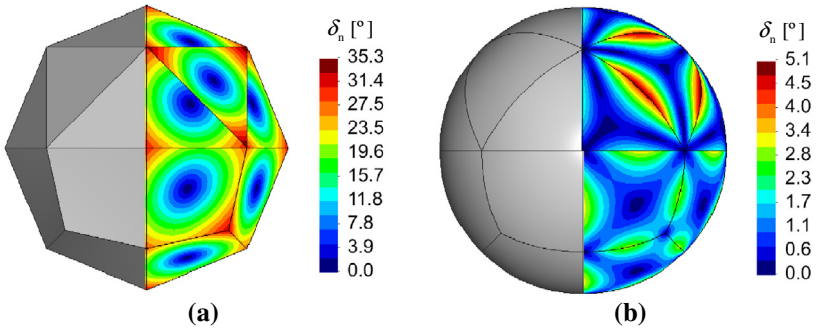

Fig. 9. Normal vector error distribution resultant from the description of a spherical surface using: (a) faceted finite elements and (b) Nagata patches.

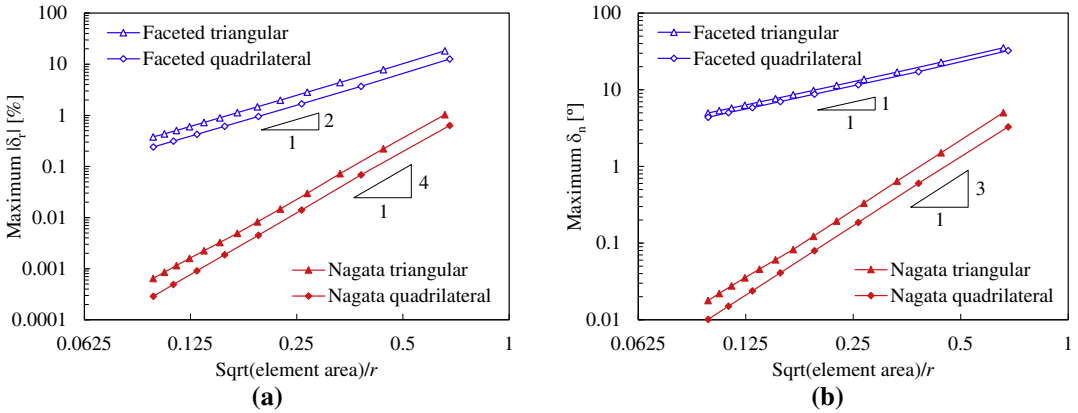

Fig. 10. Comparison of the interpolation errors in the description of a spherical surface: (a) maximum radial error modulus and (b) maximum surface normal vector error.

the maximum appears at the middle of the edges when the spherical surface is defined by Nagata patches. Besides, the vertices of smoothed surface description do not present any error since the interpolation uses the normal vectors as input parameter. This feature means that any curve described by Nagata interpolation always presents G^1 continuity.

The modulus of the maximum radial error attained in the description of the spherical surface with both faceted elements and Nagata patches is presented in Fig. 10(a). The comparison between the two surface approximations shows that the radial error modulus is significantly lower when the smoothing method is applied over the faceted description. Indeed, the maximum value of radial error decreases quartically with the square root of the element area normalized by the sphere radius [37,55]. On the other hand, the convergence rate of the maximum radial error in the faceted surface description is only quadratic, as shown in Fig. 10(a). Moreover, in both surface approximation methods, the quadrilateral elements/patches present always a maximum error inferior to the triangular typology for the same element area.

The maximum error in the surface normal vector attained by both surface description methods is presented in Fig. 10(b), for the description of a spherical surface. The comparison between the two surface approximations shows that the maximum error decrease linearly with the normalized square root of the element area when the faceted surface description is adopted, while the Nagata patches smoothing method provides a cubic rate. This cubic convergence rate allows considering that the Nagata patches smoothing method present *quasi*-G^1 continuity. For both surface approximation methods, the quadrilateral element typology presents always a maximum surface normal vector error value inferior to the triangular typology, for the same element area.

3.2. Contact search algorithm

The aim of the contact search algorithm is to quickly detect all the possible candidate contact nodes, at each increment of displacement. Therefore, the contact searching needs to be both efficient and accurate to take into account the evolution of the contact status of each slave node, along with the deformation process. Many contact search algorithms have been proposed [13,36,58–60], which are typically divided into a global and a local search process. The purpose of the global search procedure is creating a list of candidates' master facets/patches for contact with each slave node. Then the local search process is performed to determine the candidate contact point, on the contact finite element/patch. This allows the evaluation of

the signed normal distance using Eq. (5), as well as the tangential slip increment using the derivation of Eq. (6) for *quasi*-static analysis.

Among the global search algorithms proposed, the most recognized are the hierarchy-territory algorithm (HITA) [5,58], the position code algorithm [60] and the typical bucket sorting algorithm [13]. The study conducted by Oldenburg and Nilsson [60] concluded that the HITA and the position code algorithms are superior in terms of computational efficiency. While the bucket sorting algorithm performs sorting and searching in three dimensions in a nested manner, the position code reduces the three-dimensional space into a one dimensional searching problem, hence decreasing the number of operations involved due to the binary search procedure used (for more details see also [22]). Concerning the local search algorithms, several strategies can be employed such as the classic NTS approach [1,13], the pinball algorithm [59] and the inside-outside algorithm proposed in [36]. For the NTS approach, the smallest distance between each slave node and the master surface is calculated based on the projection of the node on the surface. The Newton–Raphson method is typically used to solve this problem and find the contact point coordinates. On the other hand, the pinball algorithm when combined with the penalty method is very quick since it is based on simple checks, eliminating the iteration steps. However, some inaccuracies concerning the real geometry of the two contacting bodies are introduced since the penetration between their surfaces is assumed as the interpenetration of two spherical balls. The inside-outside algorithm is based on the feature of the inside-outside status of the projected point of the node along its mesh normal direction with respect to the finite element. This algorithm is quick, robust and no iteration is required to conduct the search (closed-form expression) when faceted finite elements are used in the contact surfaces description [36].

In this study, a new contact search algorithm is developed to deal with the curved surfaces described by Nagata patches. Both the local and global search algorithms proposed are presented in the following. The global search is based on the concept of contact hierarchies suggested in [48,58], while the local search is performed with the aid of the closest point projection algorithm [34,48,61].

3.2.1. Global contact search

The numerical modeling of several frictional contact problems must take into account the large slips between the deformable body and the rigid surfaces. Thus, since the configuration of the deformable body can change somewhat arbitrarily during the process evolution, any contact node can come into contact with any patch describing the rigid contact surfaces. Therefore, it is impossible to explicitly define *a priory* the location and trace of contact areas for each contact node, in order to correctly apply the contact constraints. Hence, the proposed global contact search is divided in the following steps, schematically represented in Fig. 11.

The first step of the global contact search is performed by the user in the pre-processing phase, assigning all contact nodes (nodes with the possibility to establish contact) from the total nodes that define the deformable body. Assuming that the

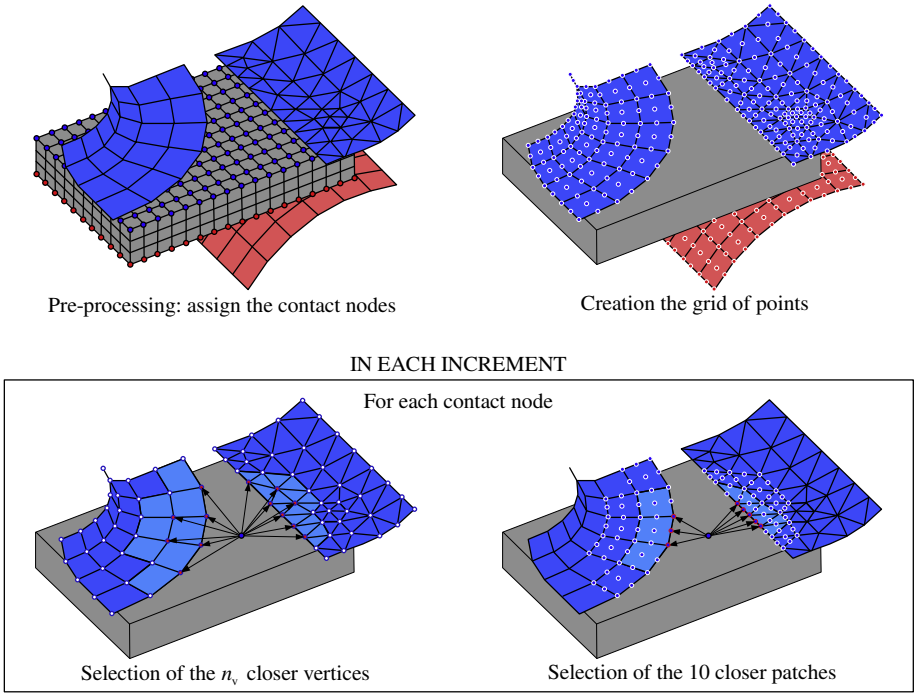

Fig. 11. Scheme of the steps composing the global contact search algorithm.

deformable body is discretized with solid finite elements, each contact node should be associated with a predefined set of rigid surfaces, based only on the orientation of each surface outward normal vector to the deformable body. Considering an example of a deep drawing process involving three tools (die, blank-holder and punch), the nodes on one face of the sheet are assigned as potential contact nodes associated to the die, while the nodes in the opposite face are associated to the blank-holder and the punch. The remaining phases of the developed algorithm are repeated in each increment of displacement since this contact search algorithm was specifically developed for solvers that use implicit integration, which are characterized by large increment size.

Depending on the quantity of rigid contact surfaces necessary to carry out the process and its geometric complexity, the amount of Nagata patches required to define accurately each rigid surface is highly variable. In complex models this number can reach several thousand as shown in the last numerical example presented in the next section. Furthermore, the opportunity to create an irregular distribution of the patches, which is more attractive from the user point of view, leads to a more complex algorithm. Indeed, the use of structured meshes in the surfaces description leads to a straightforward and efficient global search procedure, while the adoption of an unstructured mesh description conduces to more effort in the global search due to the irregular distribution of the patches. This situation is considered in the proposed algorithm introducing a parameter that expresses the topologic distortion of the patches used in each rigid contact surface. The adopted parameter r_m is defined as the maximum value of the ratio between the maximum and minimum edge length of the faceted finite elements, being independently evaluated for each contact surface involved in the numerical simulation. The value of r_m is calculated for each surface only at the beginning of the simulation, since the surface mesh is rigid.

The second step of the global contact search algorithm comprises the evaluation of the distance between each contact node (defined in first step) and every mesh vertex of the associated set of rigid surfaces. This method is sometimes referred to as the brute force approach [13]. However, in the present study its computational cost is acceptable since large increment sizes are employed and the typically problem size is not very large. After that, the global search for the closest mesh vertices to each contact node is performed to subsequently apply the inverse mesh connectivity in order to select the surrounding Nagata patches. The selected number of closest mesh vertices takes into account the topology of the surface mesh, being the number of vertices selected for each contact surface defined as follows:

$$n_v = 5 + \mathrm{int}\left(\frac{r_m^2}{65}\right), \tag{21}$$

where r_m refers to the maximum ratio between edge lengths, concerning a specific contact surface mesh. Some unstructured surface meshes present a discrepancy between finite elements area that requires a quadratic increase in the number of vertices assigned, due to the heterogeneous disposition of the patches. On the other hand, for structured meshes ($r_m \approx 1$) five vertices are sufficient to capture surface area candidate to establish contact. Therefore, this strategy allows the use a different number of vertices for each surface, guaranteeing that this number depends on the surface mesh topology. The minimum number of selected vertices in each contact surface mesh is defined as five, which is also the value used for meshes that present a ratio between edge lengths inferior to 8 in all finite elements. On the other hand, the maximum number of selected vertices was limited to 80 in order to control the computational cost of the contact search. This step ends with the identification of the Nagata patches that share the n_v closest mesh vertices, using the inverse mesh connectivity. However, since the resulting number of patches is extremely dependent on the mesh distortion, it can be computationally inefficient to directly apply the local contact search algorithm to all patches selected.

The third step of the global search algorithm involves the use of a grid of points on each Nagata patch in order to reduce the number of patches to be tested in the local contact search. The creation of the grid of points is performed only at the beginning of the numerical simulation, being the coordinates of these points updated in each increment with the rigid surfaces displacement/rotation. The grid is created from the parametric division of the Nagata patch domain, performed in both directions using uniform intervals. Hence, the number of grid divisions (number of grid points less one) in each parametric direction is defined as:

$$n_{gd} = \max\left\{2,\ \mathrm{int}\left(\frac{\max(r_m)}{10}\right)\right\}, \tag{22}$$

where $\max(r_m)$ is the maximum ratio among all discretized rigid contact surfaces involved. The number of grid points is particularly important in the presence of highly distorted finite elements, mainly for slave nodes that are located near abrupt transitions between large and small elements. The minimum number of grid divisions in each parametric direction is established as two, which represents 9 grid points for quadrilateral patches and 6 for triangular patches. The minimum amount of grid points is kept unchanged while all tool meshes involved present a r_m ratio inferior to 30, which represents a large range of distorted surface meshes. Since the grid dimension increases quadratic with the number of divisions, the maximum value allowed in each direction was limited to 6, in order to control the computational cost of the global contact search. Note that the expressions presented in Eqs. (21) and (22) are based on an extensive study using different structured and unstructured rigid surface meshes, with different complexities [62].

The last step of the proposed global search algorithm comprises the selection of the ten Nagata patches closest to the contact node. This selection is carried out evaluating the distance between the contact node and all point of each grid created on the patches identified in the second step of this algorithm. For each contact node, the ten selected patches are stored as well

as the local coordinates ξ of the closest grid point, which will be used as initial approximation for the local contact search. The sorting of the ten selected patches is not important because all of them are used in the local contact search to take into account multiple candidates. The principal steps of the proposed global contact search algorithm are summarized in the Table 1.

3.2.2. Local contact search

The objective of the local contact search is to select the appropriate candidate patch, from among the candidates previously selected in the global search, and determine the reference position $\bar{\mathbf{x}}^{(2)}$ on the selected patch, which is the location where the kinematic contact variables will be evaluated. While the global search is performed only once in each displacement increment (from line 14 to 27 of the algorithm presented in Table 1), the local search procedure is repeated in each iteration of each increment. Therefore, the local detection step can be very time consuming, particularly for large contact problems [63]. The NTS method adopted in this study is robust and accurate, even when the contact surface mesh is severely distorted, due to the use of the r_{m} parameter to control the selection of the candidates. Moreover, the grid of points constructed over the patches are used to improve the converge rate of the iterative local search procedure.

The reference position $\bar{\mathbf{x}}^{(2)}$ on the selected contact surface patch is defined as the point on the patch which is closest to the contact node $\mathbf{x}^{(1)}$. Hence, the coordinates of the reference point are evaluated determining the smallest distance between the contact node and the Nagata patch. Then, the application of the orthogonal projection algorithm [34,61] allows calculating both the reference position and the signed normal distance d^{n} by solving the following system of equations:

$$\mathbf{F}^{\mathrm{Proj}}(\bar{\xi}^1, \bar{\xi}^2, \bar{d}^{\mathrm{n}}) = \boldsymbol{P}(\bar{\xi}^1, \bar{\xi}^2) + \mathbf{u}^{\mathrm{surf}} + \bar{d}^{\mathrm{n}}\mathbf{n}(\bar{\xi}^1, \bar{\xi}^2) - \mathbf{x}^{(1)} = \mathbf{0}, \tag{23}$$

where $\boldsymbol{P}(\xi^1, \xi^2)$ denotes the Nagata patch defined in its initial location, $\mathbf{n}(\xi^1, \xi^2)$ is the outward patch normal vector and $\mathbf{u}^{\mathrm{surf}}$ is the rigid surface displacement from the beginning until the actual position. Assuming only translations of the rigid surfaces, the Nagata patch interpolation is carried out only once for the initial position of the surfaces, in order to improve the efficiency of the local contact search procedure. Afterward, the rigid surface displacement $\mathbf{u}^{\mathrm{surf}}$ is added to the interpolation coefficients $\boldsymbol{P}(\xi^1, \xi^2)$, defining the actual position of the patch as $\boldsymbol{P}(\xi^1, \xi^2) + \mathbf{u}^{\mathrm{surf}}$. The Newton–Raphson method is used for solving the non-linear system of equations, which can be summarized as follows for the $i+1$ iteration:

$$\mathbf{s}^{(i+1)} = \mathbf{s}^{(i)} - \left[\nabla \mathbf{F}^{\mathrm{Proj}}\Big|^{(i)}\right]^{-1} \mathbf{F}^{\mathrm{Proj}}\Big|^{(i)}, \tag{24}$$

Table 1
Global contact search algorithm.

	— PRE-PROCESSING —
1:	**Read** finite element mesh of deformable body
2:	**Read** finite element mesh of each rigid contact surface
3:	Definition of all contact nodes (by user)
4:	Associate each contact node to a set of rigid surfaces (by user)
	— FIRST STEP —
5:	**For** each rigid surface mesh
6:	Evaluate geometric ratio r_{m}
7:	Evaluate number of vertices n_{v} from Eq. (21)
8:	**End**
9:	Evaluate number of grid divisions n_{gd} from Eq. (22)
10:	**For** each rigid surface
11:	**For** each Nagata patch
12:	Create an uniform grid of points on the patch
13:	**End**
14:	**End**
15:	**For** each rigid surface increment
16:	**For** each contact node
	— SECOND STEP —
17:	**For** each rigid surface contained in the set
18:	**For** each vertex of the surface mesh
19:	Evaluate the distance between contact node and vertex
20:	**End**
21:	Store the n_{v} closest mesh vertices
22:	**End**
23:	Selection of Nagata patches applying inverse connectivity to the n_{v} vertices
	— THIRD STEP —
24:	**For** each Nagata patch previously selected
25:	Update the coordinates of the grid of points with rigid surface displacement
26:	Evaluate distance between contact node and points of grid
27:	**End**
28:	Selection of the 10 closest Nagata patches
29:	**End**
30:	**End**

where $\mathbf{s}^{(i)} = [\xi^{1(i)},\ \xi^{2(i)},\ d^{n(i)}]^T$ presents the solution vector at iteration i, being the required initial solution given by the closest grid point, found in the global contact search. The Jacobian matrix $\nabla\mathbf{F}^{Proj}$ of the system of equations presented in Eq. (23) is defined as follows:

$$\nabla\mathbf{F}^{Proj}(\xi^1,\xi^2,d^n) = \left[\frac{\partial}{\partial\xi^1},\frac{\partial}{\partial\xi^2},\frac{\partial}{\partial d^n}\right]\mathbf{F}^{Proj}(\xi^1,\xi^2,d^n). \tag{25}$$

The evaluation of the Jacobian matrix requires the partial derivatives of the Nagata patch and the gradient of the normal vector with respect to the local coordinates ξ^α, which can be calculated using the Weingarten formula [15,34,45]:

$$\frac{\partial\mathbf{n}}{\partial\xi^\alpha} = -m^{\sigma\gamma}(\xi^1,\xi^2)k_{\gamma\alpha}(\xi^1,\xi^2)\boldsymbol{\tau}_\sigma(\xi^1,\xi^2), \tag{26}$$

where $m^{\sigma\gamma}$ denotes the surface contravariant components and $k_{\gamma\alpha}$ represents the components of the symmetric curvature tensor, defined as follows:

$$k_{\gamma\alpha}(\xi^1,\xi^2) = \boldsymbol{\tau}_{\gamma\alpha}\cdot\mathbf{n}, \tag{27}$$

which is obtained as the dot product of the second derivative of the patch $\boldsymbol{\tau}_{\gamma\alpha}$ and the normal vector $\mathbf{n}$.

In order to reduce the computational cost of the iterative process presented in Eq. (24), the maximum number of iterations is taken as 10. In most of the cases, the quadratic definition of the Nagata patches allows finding the solution with a very small tolerance using a small number of iterations (less than 4). Furthermore, the quadratic convergence of the Newton–Raphson method is attained due to the initial solution delivered by the grid of points, introduced in the global search. Also, the *quasi-*G^1 continuity in the contact surfaces description (attained with the Nagata patches) avoids numerical instabilities in the global iterative procedure (Eq. (11)), which normally occurs for faceted surfaces due to the severe discontinuity of the normal vector field across the finite elements. However, the arising of multiple contact possibilities for the contact node, i.e. several Nagata patches fulfilling the convergence criterion, can result in multiple solutions for the reference point. This situation affects highly the efficiency of the contact searching since all solutions should be verified. Therefore, the projection algorithm expressed by Eq. (23) is applied to each of the ten Nagata patches selected in the global contact search. In case of multiple solutions, the reference point with the minimum normal distance to the contact node is selected as the solution. Another advantage of using the Nagata patch combined with the projection algorithm is that the 'deadzone' problems, which arise when curved rigid surfaces are discretized by low order finite elements, are consequently eliminated. In fact, the *quasi-*G^1 continuity of the surface created with Nagata patches ensures that even close to the patch edges the solution of the projection algorithm is successfully attained.

3.3. Contact kinematic variables evaluation

Once the reference position $\bar{\mathbf{x}}^{(2)}$ is evaluated, the local frame system used to calculate the contact variables is defined by the rigid surface patch normal vector $\bar{\mathbf{n}}^{(2)} \equiv \mathbf{n}(\bar{\xi}^1,\bar{\xi}^2)$ at this reference point, which is not constant during the iterative equilibrium loop. The signed normal distance and the slip increment are the kinematic contact variables necessary to define the relative displacement between the contact nodes and the rigid surfaces. While the signed normal distance $\bar{d}^n$ is obtained directly from the projection algorithm, by solving Eq. (23), the evaluation of the tangential slip increment requires an appropriate definition of the reference position at the prior equilibrium step. Hence, from the definition of the tangential slip velocity presented in Eq. (6), the associated tangential component of the slip increment can be written as:

$$\boldsymbol{\delta}^t = \boldsymbol{\delta} - (\boldsymbol{\delta}\cdot\bar{\mathbf{n}}^{(2)})\bar{\mathbf{n}}^{(2)}, \tag{28}$$

where the normal vector $\bar{\mathbf{n}}^{(2)}$ used to split the slip increment into normal and tangential components is evaluated at the solution point of the projection algorithm $(\bar{\xi}^1,\bar{\xi}^2)$. The slip increment $\boldsymbol{\delta}$ is defined as the vector connecting the reference point in the prior equilibrium step (updated with the incremental rigid surface displacement) and the contact node position in the current increment. Fig. 12 presents a 2D scheme illustrating the definition of both kinematic variables $\boldsymbol{\delta}$ and d^n for the two possible contact status (gap or contact) of the contact node at the prior equilibrium step. Since the reference position calculated in the prior equilibrium step is necessary to the current increment, its position vector is updated with the incremental surface displacement $\Delta\mathbf{u}^{surf}$ at the current increment, being the updated reference position defined as $\bar{\mathbf{x}}'^{(2)} = \bar{\mathbf{x}}^{(2)} + \Delta\mathbf{u}^{surf}$. When the contact node is in contact with the rigid surface in the prior equilibrium step, the reference point in that step is coincident with the contact node, as depicted in Fig. 12(a). Therefore, the slip increment $\boldsymbol{\delta}$ is accurately defined through the updated reference position of the prior equilibrium step $\bar{\mathbf{x}}'^{(2)}$ and the current position of the contact node $\mathbf{x}^{(1)}$, being given by $\boldsymbol{\delta} = \mathbf{x}^{(1)} - \bar{\mathbf{x}}'^{(2)}$. However, in the case that the contact node gets into contact during the current increment (Fig. 12 (b)), the definition of the reference position required to evaluate the slip increment is not trivial. In this study, the procedure proposed by Heege and Alart [34] is adopted, which is based on the projection of the contact node in the prior equilibrium step on the rigid surface. Thus, the reference position obtained in the prior equilibrium step is updated with the incremental surface displacement in order to obtain the slip increment given by $\boldsymbol{\delta} = \mathbf{x}^{(1)} - \bar{\mathbf{x}}'^{(2)}$, as shown in Fig. 12(b).

Since it is used a single iterative loop to solve both nonlinearities related with the mechanical behavior and the frictional contact, both the position vector of the contact nodes and the local frame system defined by the outward normal vector can

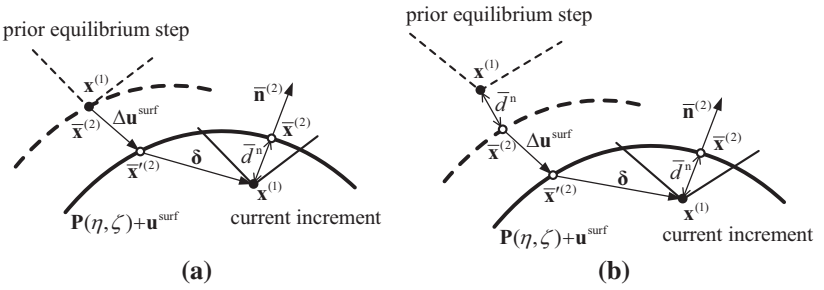

Fig. 12. Definition of the contact kinematic variables when the contact node $\mathbf{x}^{(1)}$ in the prior equilibrium step is: (a) in contact the rigid surface and (b) not in contact with the rigid surface.

vary during the iterative solution. Therefore, the evaluation of the kinematic variables for each node candidate to establish contact, with admissible solution for the reference position arising from the local contact search, should be updated in each iteration within the incremental solution of the equilibrium equations.

4. Numerical examples

The algorithm presented in Section 3.1 developed to smooth finite element mesh surfaces by means of Nagata patches has been implemented in the DD3IMP in-house finite element code [39]. Furthermore, the new contact search algorithm, specifically developed to model the contact between a deformable body and rigid contact surfaces described by Nagata patches (see Section 3.2), has also been introduced in this in-house code. In this section, two simple academic frictional contact examples and an industrially sheet metal forming example are chosen to demonstrate the accuracy, efficiency and robustness of the proposed algorithms. All numerical simulations are carried out with the DD3IMP code, on a computer machine equipped with an Intel® Core™ i7–2600 K Quad-Core processor (3.4 GHz) and the Windows 7 Professional (64-bits platform) operating system.

The smoothing method proposed is compared with the traditional faceted surface description, both in terms of numerical results and computational performance. Nevertheless, since the faceted rigid surface description is not available in DD3IMP finite element code, the comparison is carried out using the finite element mesh described by linear Nagata patches. Thus, the curvature parameter defined in Eq. (14) is taken as zero, meaning that the information regarding the surface normal vectors is not used in the interpolation.

4.1. Ironing problem

This simple example consists in sliding a rigid cylindrical die along a deformable slab (see Fig. 13), which is inspired in the one proposed by Puso and Laursen [20]. The slab dimensions are $9 \times 4 \times 3$ and the die has 5.2 wide with a radius of 3. The slab is discretized using 8-node hexahedral solid finite elements, combined with a selective reduced integration (SRI) technique, commonly used in contact problems [64,65]. Moreover, it is assumed to be elastic to focus the analysis on the interface behavior, being the Young's modulus and Poisson's ratio taken as $E = 1$ and $\nu = 0.3$, respectively. The friction is modeled using Coulomb's law with $\mu = 0.1$. The cylindrical die, with the center initially located 2.5 units from the left end of the slab,

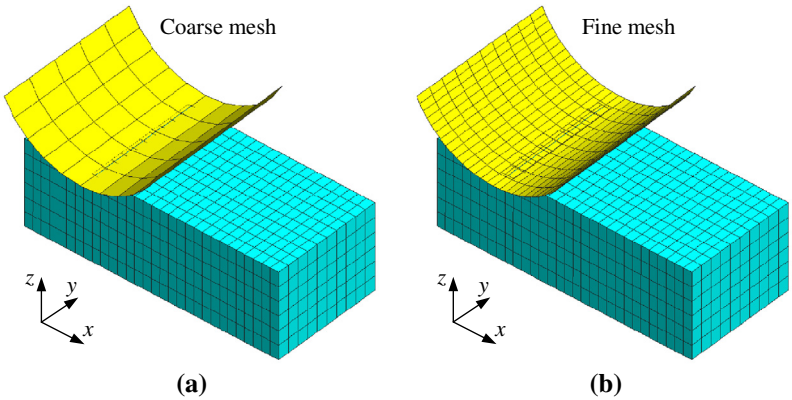

Fig. 13. Definition of the ironing problem: (a) cylindrical die described by a coarse mesh and (b) cylindrical die described by a fine mesh.

travels −1.0 units in the vertical z-direction and then 4 units in the horizontal x-direction, while the slab is fixed on the bottom. The vertical displacement of the die in the z-direction is divided into 10 equal increments, while the horizontal displacement in the x-direction is divided into 100 increments, being these increment sizes imposed in all simulations. Two distinct structured meshes composed by quadrilateral elements are adopted in the discretization of the cylindrical die, a coarse mesh and a fine mesh, as shown in Fig. 13(a) and (b), respectively. The number of elements used in each mesh is indicated in Table 2, as well the maximum radial error verified for each surface description method.

The cylindrical die force evolution with its displacement in the x-direction is presented in Fig. 14, for both faceted and smoothed die descriptions. When using the traditional faceted elements for the master surface description, the selection of the fine mesh reduces the chatter effect in the die force, as a result of the reduction of the radial error in the die description (see Table 2). However, the chatter effect is not completely eliminated since the radial error is still relevant, which leads to overestimation of the contact force. On the other hand, the application of the smoothing method to any of the die meshes (coarse and fine) leads to important improvements in the die force evolution, particularly the elimination of the chatter effect. Indeed, the application of the smoothing operation in both meshes lead exactly to the same die force evolution. The slight oscillations observed in the die force evolution obtained with the smoothing method are related with the deformable body discretization.

Table 2 presents the comparison of the computational performance between the faceted and the smoothed surface description methods. Although the number of increments is the same in all simulations, during the displacement of the die in the x-direction the average number of iterations required for each increment is higher when using the faceted description. This is associated with the poorer geometric description of the rigid die, both in terms of shape and normal vector distribution. Indeed, for the faceted description, the required number of iterations is higher in the fine mesh than in the coarse one, despite the inferior value of the maximum radial error attained by the fine mesh. This can be explained by the fact that the fine mesh combines a substantial discontinuity of the normal direction between facets with a higher number of facets, which the slave nodes need to cross. On the other hand, both the elapsed real time and the average number of interactions necessary to carry out the simulation is independent of the rigid die discretization when the smoothing method is applied, as shown in Table 2.

4.2. Cylindrical contactor sliding in a half-tube

The second example comprises a cylindrical contactor sliding in a half-tube, which is a simplification (rigid-deformable instead of deformable-deformable) of the academic example proposed by Krstulovic-Opara et al. [26]. The cylindrical contactor dimensions are $2 \times 2 \times 2$ with the curvature radius of $r = 3$ in the contact surface (see Fig. 15). The cylindrical contactor is discretized using hexahedral solid finite elements (SRI) and modeled with elastic behavior, being the Young's modulus and

Table 2
Geometric characteristics of the cylindrical die and computational performance of both surface description methods, when applied to the ironing problem.

	Faceted description		Smooth description	
	Coarse mesh	Fine mesh	Coarse mesh	Fine mesh
No elements/patches	50	300	50	300
Max radial error (%)	0.6295	0.070	0.00236	0.00016
Avg. no of iterations (horizontal disp.)	6.29	7.12	5.10	5.10
Elapsed time (s)	46	52	38	38

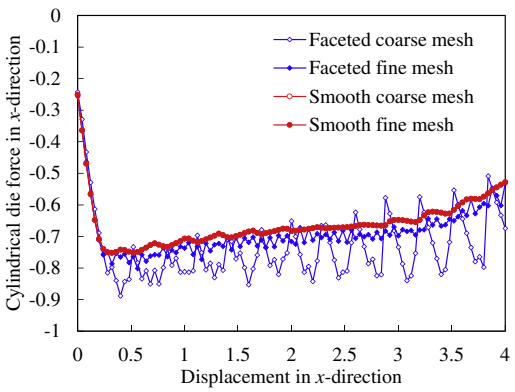

Fig. 14. Influence of the smoothing method in the cylindrical die force evolution with its displacement in x-direction.

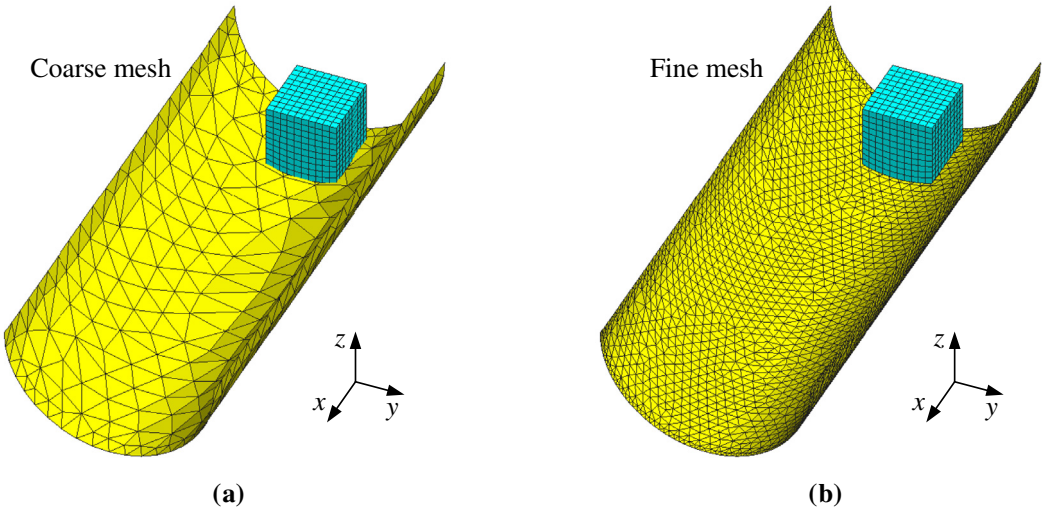

Fig. 15. Definition of the cylindrical contactor sliding in a half-tube described by a: (a) coarse mesh and (b) fine mesh.

Poisson's ratio taken as $E = 100$ and $\nu = 0.3$, respectively. The half-tube has a radius of $r = 3$ and 15 units of length. The friction behavior is modeled using the Coulomb's law with $\mu = 0.1$. The contactor is pressed into the half-tube with an overlapping of $\delta = 0.01$ and then a displacement of 10 units, in the x-direction from the position shown in Fig. 15 is applied at the contactor's upper surface, while the half-tube is clamped. In order to accurately capture the possible oscillations in the contactor force evolution, the imposed displacement on the contactor is divided into 100 equal increments. In this example the rigid half-tube is discretized by an unstructured mesh composed by triangular finite elements. As in the previous example, two distinct meshes are studied, a coarse mesh and a fine mesh, as shown in Fig. 15(a) and (b), respectively. The number of finite elements used in each discretization is indicated in Table 3, as well the maximum radial error attained in each surface description method.

Fig. 16(a) presents the cylindrical contactor force evolution in the x-direction with its displacement, comparing the results obtained with the smoothing method with the ones attained with the faceted surface description. From the analysis of Fig. 15(a) and Table 3 it is possible to conclude that the coarse faceted mesh of the half-tube leads to a bad approximation of the cylindrical geometry, being this directly reproduced in the contactor force evolution. The improvement in the predicted contact force evolution with the application of the smoothing method to this mesh is evident, demonstrating its benefit. Also, despite the huge improvement in the force prediction when the coarse mesh is replaced by the fine mesh in the faceted description, the evolution obtained by the smoothing method is not reached, as shown in Fig. 16(a). Although, the maximum radial error of the smoothed coarse mesh and the faceted fine mesh is similar (see Table 3), the smooth description attains this maximum in small local areas while the error distribution for the faceted fine mesh is almost uniform. Furthermore, the faceted surface description leads to a cylindrical geometry with an effective radius always inferior to the analytical one, leading to the force increase. On the other hand, the application of the proposed smoothing method leads to approximately the same force evolution for both half-tube surface meshes studied.

The evolution of the number of slave nodes in contact with the surface defining the half-tube is presented in Fig. 16(b), for both rigid surface description methods (faceted and smooth). Only the coarse mesh associated with the faceted surface description leads an evolution completely different, similarly to what happens for the contactor force evolution. The number of slave nodes in contact is about 80 (accompanied with some oscillations) for the coarse faceted mesh, while the remaining models present an evolution more stable with approximately 121 nodes in contact, which is the total of slave nodes (contactor discretization with $10 \times 10 \times 10$ elements). The number of nodes in contact dictates directly the stress distribution induced in the deformable body, since contact forces only arise in the nodes in contact, being an important parameter to take into account to achieve accurate results.

The comparison of the computational performance between the faceted and the smoothed surface description methods is presented in Table 3. In this example the average number of iterations required in each increment is only slightly affected by

Table 3
Geometric characteristics of the cylindrical contactor and computational performance of both surface description methods, when applied to the contactor sliding in a half-tube problem.

	Faceted description		Smooth description	
	Coarse mesh	Fine mesh	Coarse mesh	Fine mesh
No elements/patches	486	3880	486	3880
Max radial error (%)	3.43	0.263	0.208	0.063
Avg. no of iterations	5.37	5.05	5.04	5.00
Elapsed time (s)	27	36	25	33

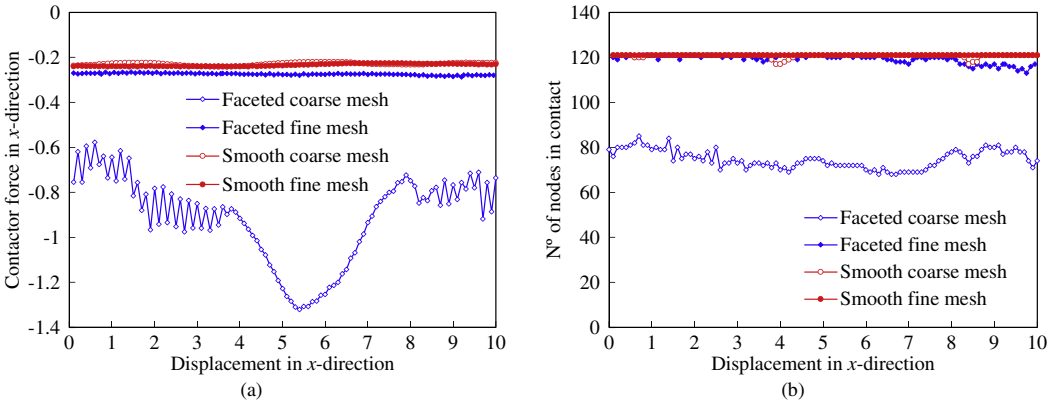

Fig. 16. Comparison between the faceted and the smooth mesh description in the cylindrical contactor sliding in a half-tube: (a) cylindrical contactor force with its displacement and (b) number of nodes in contact with the half-tube.

the surface description method, being higher in the traditional faceted description. In fact, only the coarse mesh defined with facets leads to a clearly higher number (5.4 iterations), in comparison with the other models that require about 5 iterations. Although the number of iterations is similar, the elapsed real time necessary to carry out the simulation is highly variable between models. This discrepancy is associated with two factors: the number of elements in the discretization of the rigid half-tube and the accuracy in its geometric description. Regardless of the surface description method applied, the elapsed time increases when using the fine mesh model due to the higher number of finite elements used in its description, as specified in Table 3. The smoothing method results always in a decrease of the required elapsed time, as a result of the improved accuracy. Note that the performance results for the coarse mesh cannot be directly compared with the others, since the predicted process conditions are completely different.

4.3. Automotive underbody cross member panel

The selected example consists in the sheet metal forming process of an automotive underbody cross member panel, which was proposed as benchmark at the Numisheet 2005 conference [66]. The large dimensions of the component and the complexity of tools geometry dictate the use of a very large number of finite elements in the description of the sheet in order to describe accurately the process and particularly the frictional contact conditions (assign contact status). The numerical simulation of the stamping process consists of three operations: (i) forming, (ii) trimming and (iii) springback. Nevertheless, only the first operation is performed in this study since the forming stage dictates the success of the next operations and it is largely affected by the contact surface description. The forming process involves three rigid tools and can be decomposed into two phases: blank-holder clamping until 1068 kN and consequent punch displacement until 100 mm, while maintaining the clamping force constant. The geometry of the tools includes physical drawbeads to control material flow, which highly increase its geometric complexity. The selected material for the sheet is a DP600 dual-phase steel with an initial thickness of 1.62 mm, as proposed by the benchmark committee [67].

Due to geometric and material symmetry conditions at $y = 0$, only half model is considered in the simulation, as shown in Fig. 17. Regarding the material mechanical behavior, the isotropic work hardening is assumed to be described by the Swift law, while the orthotropic behavior is described by the Hill's 1948 yield criterion. The material parameters were obtained from the experimental data provided by the benchmark committee [67] and are presented in Table 4. The friction coefficient

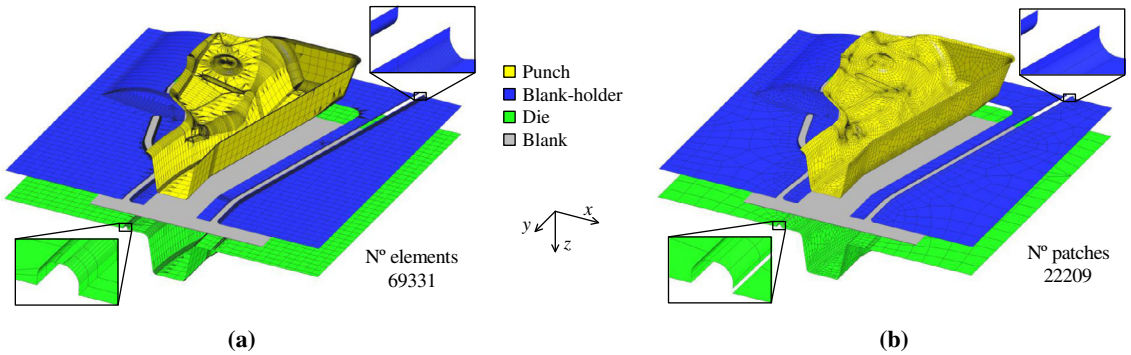

Fig. 17. Half model with the tool surfaces described by: (a) faceted finite elements and (b) quadratic Nagata patches.

Table 4
Material properties of the dual-phase steel DP600.

Elastic properties		Swift law $Y = K(\varepsilon_0 + \bar{\varepsilon}^p)^n$			Hill'48 criteria					
E (GPa)	ν	Y_0 (MPa)	K (MPa)	n	F	G	H	L	M	N
206	0.3	393.0	1038.8	0.162	0.460	0.576	0.424	1.500	1.500	1.446

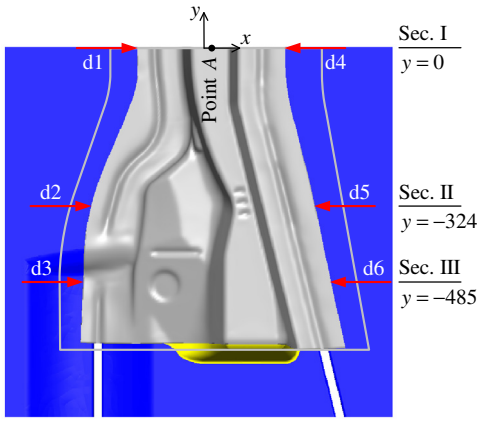

Fig. 18. Sections for the blank draw-in and thickness measurement and identification of point A.

between the sheet and the tools is taken from the benchmark instructions as $\mu = 0.12$. The blank geometry (half model), is shown in Fig. 18 and can be defined by its width in x direction of 620 mm and length in y direction of 607 mm. It is discretized with 8-node hexahedral solid finite elements, combined with SRI technique. The total number of solid elements is $180 \times 150 \times 2 = 54{,}000$, using 2 layers of elements through the thickness. Concerning the tools description, the information about the tools geometry was provided by the conference committee both in a Nastran mesh file and in an IGES format file. The available Nastran mesh is composed by a mixture of triangular and quadrilateral finite elements, as shown in Fig. 17(a). This discretization was generated to use directly in the numerical simulation without any type of additional surface smoothing procedure. On the other hand, the IGES file of each tool is used in this study to create the discretized tool surfaces, which are smoothed with quadratic Nagata patches and posteriorly applied in the numerical analysis. Fig. 17(b) presents the model of the forming tools described by Nagata patches. The principal features of each tool model are indicated in Table 5, comparing both the number of vertices and the number of finite elements/Nagata patches used to describe each forming tool. Note that the total number of finite elements is approximately three times higher in the Nastran mesh than the number of Nagata patches applied in the description of all tool surfaces, being the faceted tool model characterized by a mesh refinement in all curved surfaces. Since the smoothing method improves significantly the geometric accuracy of the discretized tool surfaces, the comparison is performed between a refined faceted tool mesh and a coarse smoothed tool mesh, both with similar level of geometric accuracy.

Although the proposed surface smoothing method allows applying simultaneously both triangular and quadrilateral patches, the last type of patches was selected to describe all tool surfaces. Indeed, the unstructured mesh topology was adopted to discretize the tool surfaces due to its easy and fast generation. This discretization was generated automatically using the personal pre-processor GiD [68], employing the chordal error option to assign the finite element size. The required parameter corresponds to the maximum relative chordal error (chordal error of an element divided by its characteristic size) in the whole model, which was taken as 7% to create at least two elements in the discretization of each quarter of circle arc (cf. Fig. 7 with a normalized arc length of 0.78). Additionally, the drawbeads geometry was described using a structured mesh in order to improve the accuracy attained in the subsequent smoothing stage. The drawbeads definition is a very important issue in the treatment of frictional contact problems due to the high contact forces involved and the large slip between the sheet and the tools. Typically the drawbeads geometry is approximately cylindrical, which allows the easy assessment of the geometric error introduced by the surfaces discretization procedure. In the present example, each quarter of the cylinder defining the drawbeads is described by 2 Nagata patches in the circumferential direction (see details in Fig. 17), leading to a maximum radial error (positive) inferior to 0.32%, as shown in Fig. 7 for the circular geometry. On the other hand, the tool model defined using faceted finite elements contains 12 and 16 finite elements in the circumferential direction of each quarter of cylinder (see details in Fig. 17) that composes the drawbeads of the die and blank-holder, respectively. This surfaces discretization leads to a maximum radial error (negative) of approximately 0.2% and 0.12% in the description of the drawbeads geometry inserted in the die and blank-holder, respectively (cf. Fig. 7, linear interpolation with a normalize arc length of 0.13 and 0.098). Therefore, the drawbeads model composed by faceted finite elements is slightly

Table 5
Number of vertices and finite elements/Nagata patches used to describe each forming tool in both models.

Tool	Faceted surfaces description		Smooth surfaces description	
	No vertices	No finite elements	No vertices	No Nagata patches
Punch	23397	24644	9660	9483
Blank-holder	9769	9833	1947	1733
Die	32743	34854	11279	10993
Total	65909	69331	22886	22209

more accurate in terms of shape than the geometry defined by Nagata patches. However, the linear finite element discretization leads to sudden changes in the surface normal field among 5.5° and 7.5°, whereas a continuous surface normal field is attained using Nagata patches in the surface description.

4.3.1. Results and discussion

The first phase of the forming process comprises the blank-holder clamping using a force of 1068 kN. In order to correctly position the punch to the next phase, the punch and blank-holder move together during this phase. Fig. 19(a) presents the blank-holder force evolution with its displacement for both the smooth and the faceted tool surfaces descriptions. Since the bending effects play a dominant role during the blank-holder closure, the blank-holder force evolution is nearly independent of the strategy adopted to describe the forming tools, as shown in the figure. Indeed, the sliding between the sheet and the tools is small during this phase, which yields similar tool force evolutions. Until approximately 23 mm of blank-holder displacement the contact between the sheet and the tool surfaces is established locally, being the effective clamping accomplished in the last 5 mm of displacement. The second phase of the forming process involves the displacement of the punch, keeping the holding force of the blank-holder constant. The punch force evolution obtained for both strategies adopted to describe the tool surfaces is presented in Fig. 19(b). The occurrence of sliding between the sheet and the drawbeads during the punch movement becomes important in this second phase. Nevertheless, negligible differences are observed in the punch force evolution, since the tool geometry accuracy is similar for both models. The exponential growth of the punch force observed at the end of the forming process is related with the closing of the sheet between the punch and the die. The only experimental data available is the maximum force attained by the die, being its value 6226 kN [69], which can be defined numerically as the sum of the punch and blank-holder forces. However, the maximum force reached is very sensitive to the total punch displacement, due to the high force gradient at the end of the process (see Fig. 19(b)). Therefore, this parameter is inadequate to verify the accuracy of the numerical results. The oscillations observed in the force evolution for both tool description strategies are due to numerical instabilities related to the ratio between the blank mesh element size and the curvature radius of the drawbeads, precluding the accurate definition of the frictional contact. Since the minimum radius in the tool geometry is about 4.5 mm, to avoid such problems the mesh size should be lower than 1 mm [11]. However, this small element size leads to impracticable computational times, being the mesh size used in this study about 3 mm to overcome this limitation. Fig. 20 presents the flow stress distribution on the cross member panel at the end of forming operation, as predicted by the model that uses faceted finite elements in the tool description (see Fig. 20(a)) and using the smooth tool surface description (see Fig. 20(b)). As a consequence of the material flow between

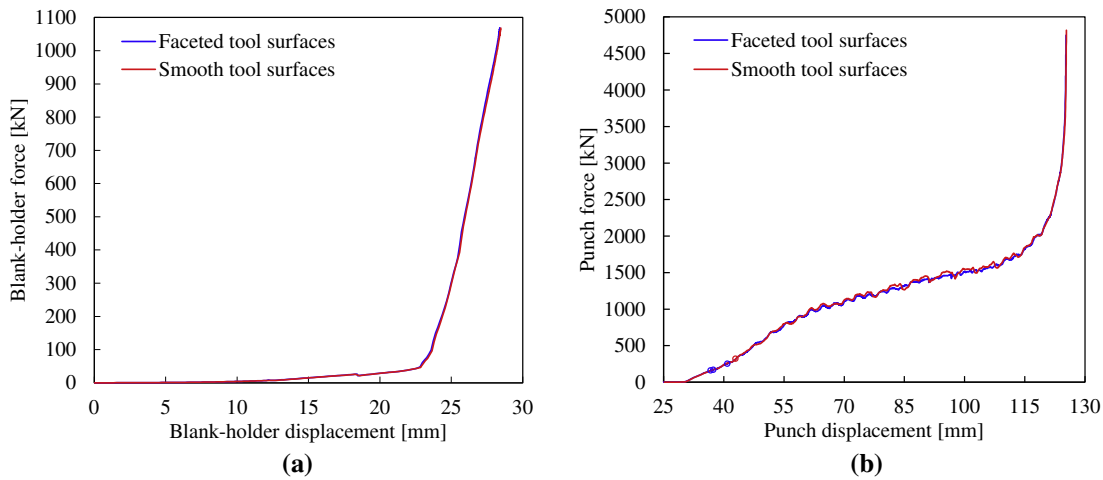

Fig. 19. Comparison of the tool force evolution between the faceted and smooth tool surface description methods: (a) blank-holder force and (b) punch force.

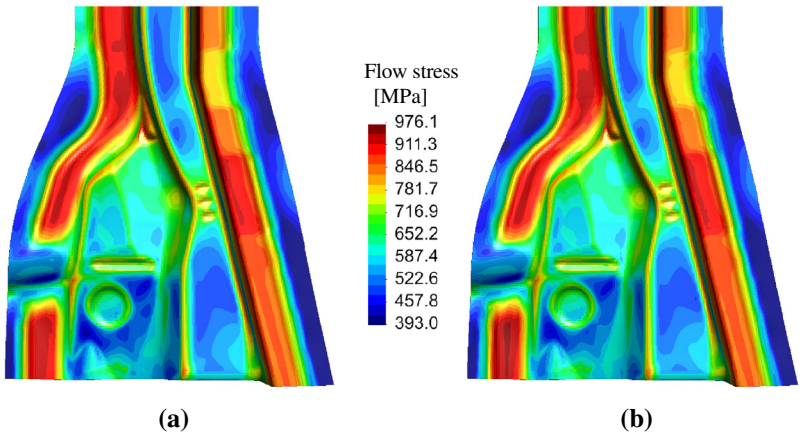

Fig. 20. Predicted flow stress distribution after forming operation using in the tool surface described by: (a) faceted finite elements and (b) smooth Nagata patches.

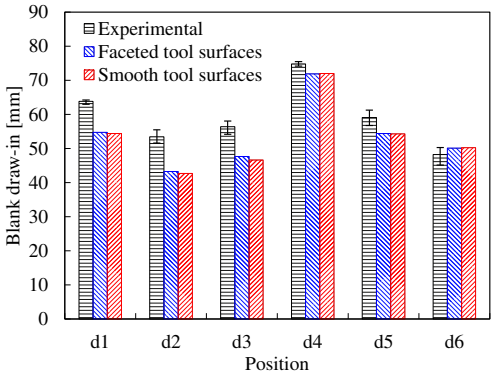

Fig. 21. Comparison between experimental and numerical blank draw-in amount at specific localizations after forming (identified in Fig. 18).

the drawbeads, the higher values of flow stress arise in the regions around them, highlighting the bending-unbending effect induced by the drawbeads in the sheet. Both tool description methods lead to a similar predicted flow stress distribution since the tool geometry accuracy is approximately the same in both models.

The two parameters selected in this study to evaluate the accuracy of the numerical results are the ones proposed in the benchmark specifications [66]. Fig. 21 presents the comparison between experimental and numerical draw-in amount at the six positions predefined in Fig. 18. Globally, the numerical prediction of the draw-in amount underestimates the experimental values, mainly in the left side of component (positions d1, d2 and d3). The maximum difference in the numerical simulation occurs at position d2, being its value around 20%. In fact, the lower draw-in amount predicted is related with the artificial roughness introduced by the coarse mesh adopted for the sheet, which hampers the material flow through the drawbeads. Since the accuracy of the tool geometry is identical in both surface tool models, the draw-in amount predicted in the numerical simulation is also similar, being slightly higher for the faceted tool description due to the negative radial error in the drawbeads regions. In fact, the positive radial error observed in these regions for the smoothed surfaces corresponds to a slight decrease of the gap between the die and blank-holder and hence inhibits the material flow. The thickness distribution at the symmetry plane (Section I) after forming is presented in Fig. 22, were the numerical results are compared with the experimental one. The experimental tendency of the thickness distribution is well reproduced numerically, despite being underestimated in all points of the section. The strong relation between the draw-in and the thickness accuracy can be verified through the comparison of Figs. 21 and 22, being this positive correlation also referenced in [70]. The difference between numerical and experimental thickness distribution is globally inferior to 5%, except in the fillet edge region located at an arc-length distance from point A ($x = 7$) around 33 mm (see Fig. 22), where the difference is roughly 7%. Both numerical distributions obtained are identical for the same reasons previously mentioned.

The computational efficiency of the proposed surface smoothing method, when compared with the traditional faceted description method, is shown in Table 6 by means of both the elapsed real time and the necessary number of increments to carry out the simulation. The number of increments with its size reduced and the simulation run errors, caused by convergence problems during the iterative loop, was selected in this study to indicate the robustness of the tool surfaces

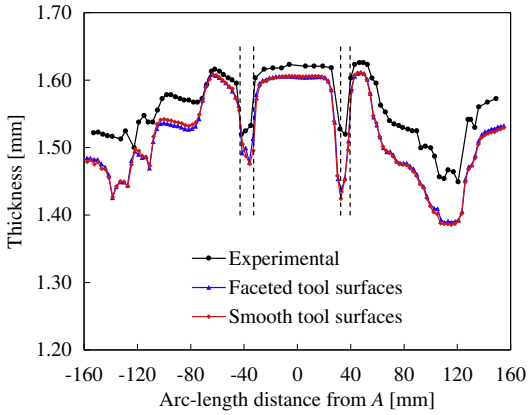

Fig. 22. Comparison between experimental and numerical thickness distribution at the symmetry plane (Sec. I in Fig. 18) after forming.

Table 6
Comparison of both performance and robustness between the smooth and faceted tool surface description methods, evaluated in each phase of the forming process.

Tool model	Blank-holder clamping				Punch displacement			
	Elapsed time (h)	No increments	Increment size reductions	Run errors	Elapsed time (h)	No increments	Increment size reductions	Run errors
Faceted tool surfaces	12.6	368	32	0	134.2	1919	1120	3
Smooth tool surfaces	7.1	352	19	0	16.9	1106	120	1

description method. Indeed, the called *NTrial* strategy currently implemented in DD3IMP code allows overcoming must of the convergence problems by automatically reducing the increment size, when convergence is not attained within the allowed number of iterations. The results show that the number of increments required to complete the blank-holder clamping phase is slightly lower when the smooth surface description is adopted. Nevertheless the elapsed real time spent is reduced to almost half using smooth tool surfaces. Therefore the computational time consumed in each increment is lower, which can be related with the smaller number of patches used to describe the tool surfaces (cf. Table 5), becoming the global search procedure computationally less expensive. In fact, the surface mesh provided in Nastran format presents a high ratio between the finite element edges length r_m, leading to the maximum values allowed for the number of vertices and number of grid divisions, expressed in Eqs. (21) and (22), respectively. No convergence problems arise in the simulation during this phase for neither tool description methods, since there is small sliding between the sheet and the tools. Concerning the drawing phase, the elapsed real time necessary to carry out this second phase is much lower when the smoothed surface description is applied, being reduced from about 134 to only 17 h. This is a consequence of the reduction in the number of increments required from 1919 to 1106 when the proposed surface smoothing method is adopted. The convergence problems observed in the faceted model are justified by the surface normal changes, which are drastically reduced with the smoothing method. Hence, the number of increments with its size reduced by the *NTrial* strategy is 1120, when the faceted tool surface description method is applied, being this value reduced to only 120 increments when the surfaces are smoothed with Nagata patches, as presented in Table 6. Therefore, the computational time reduction observed with the adoption of the proposed smoothing method is related with two factors: lower number of required increments and global contact search procedure computationally less expensive. Moreover, during the punch displacement phase some run errors occur in the finite element simulation caused by convergence problems, which cannot be solved by simply changing the increment size. This is indicated by the hollow circle symbol in Fig. 19(b). Only one run error occurred with the presented smoothing method, while the faceted tool description presented three errors. These run errors require the user intervention in order to change the penalty parameter and resume the simulation.

5. Conclusions

A new smoothing method for discretized 3D contact surfaces has been developed and implemented in DD3IMP in-house finite element code. The proposed method adopts quadratic Nagata patches to interpolate the finite element surface mesh using only the position and normal vectors at the nodes, providing an accurate and smooth description of the contact surfaces. Since the Nagata patch interpolation possesses local support characteristic, the applicability of the presented smoothing method to mixed unstructured meshes is straightforward, ensuring the description of 3D contact surfaces of arbitrary

mesh topology. Despite the low order interpolation of the Nagata patches, the G^1 continuity in the mesh nodes and *quasi*-G^1 between patches is always satisfied in the resulting smoothed surfaces. Therefore, this surface description method leads to superior convergence rate in the non-linear finite element solution of frictional contact problems, mainly in numerical simulations involving large sliding between the bodies. Moreover, a new efficient contact search algorithm was developed to identify, for each slave node, the Nagata patch local coordinates of its counterpart contact point.

The numerical examples selected to illustrate the main features of the proposed contact surface smoothing method comprise two academic examples of frictional contact and the sheet metal forming of an automotive panel. The numerical results show significant improvements in terms of efficiency, robustness and accuracy when the smoothing method is adopted to solve contact problems, when compared with the traditional faceted finite element meshes. The improvement in the geometric description of the contact surfaces, particularly the surface normal vector field, eliminates the oscillations in the contact force, even when the contact surface is discretized with a relatively coarse mesh. Indeed, the numerical results are almost independent of the mesh used to discretize the rigid master surfaces, when the smoothing method is applied. The lower number of Nagata patches required to accurately describe the contact surfaces reduces the computational time consumed in the global contact search algorithm, when compared with the traditional faceted finite element meshes.

Regarding the studied industrial example, the computational time required to complete the simulation using the smoothing method is roughly 6 times less than the one obtained when adopting the traditional faceted surface description. This superior computationally efficiency is directly correlated with the higher robustness attained in the frictional contact treatment provided by the smoothing method. Indeed, the number of increments necessary to complete the drawing phase is reduced to almost half when smooth tool surfaces are used, since the increment size is automatically reduced, through the *NTrial* strategy, in order to overcome the convergence problems that arise when using faceted elements.

Acknowledgments

The authors gratefully acknowledge the financial support by FEDER funds through the program COMPETE (FCOMP-01-0124-FEDER-010301) and by national funds through the Portuguese Foundation for Science and Technology (FCT) under the projects with reference PTDC/EME-TME/103350/2008 and PEst-C/EME/UI0285/2011. The first author is also grateful to the FCT for the Ph.D. Grant SFRH/BD/69140/2010.

References

[1] J.O. Hallquist, G.L. Goudreau, D.J. Benson, Sliding interfaces with contact-impact in large-scale Lagrangian computations, Comput. Methods Appl. Mech. Eng. 51 (1985) 107–137.
[2] P. Wriggers, T.V. Van, E. Stein, Finite element formulation of large deformation impact-contact problems with friction, Comput. Struct. 37 (1990) 319–331.
[3] J.C. Simo, T.A. Laursen, An augmented Lagrangian treatment of contact problems involving friction, Comput. Struct. 42 (1992) 97–116.
[4] T.A. Laursen, J.C. Simo, A continuum-based finite element formulation for the implicit solution of multibody large deformation frictional contact problems, Int. J. Numer. Methods Eng. 35 (1993) 3451–3485.
[5] Z.H. Zhong, Finite Element Procedures for Contact-Impact Problems, Oxford University Press, Oxford, 1993.
[6] P.W. Christensen, A. Klarbring, J.S. Pang, N. Strömberg, Formulation and comparison of algorithms for frictional contact problems, Int. J. Numer. Methods Eng. 42 (1998) 145–173.
[7] L. De Lorenzis, P. Wriggers, G. Zavarise, A mortar formulation for 3D large deformation contact using NURBS-based isogeometric analysis and the augmented Lagrangian method, Comput. Mech. 49 (2012) 1–20.
[8] P. Alart, A. Curnier, A mixed formulation for frictional contact problems prone to Newton like solution methods, Comput. Methods Appl. Mech. Eng. 92 (1991) 353–375.
[9] A.L. Eterovic, K.J. Bathe, On the treatment of inequality constraints arising from contact conditions in finite element analysis, Comput. Struct. 40 (1991) 203–209.
[10] P. Papadopoulos, R.L. Taylor, A mixed formulation for the finite element solution of contact problems, Comput. Methods Appl. Mech. Eng. 94 (1992) 373–389.
[11] L. Taylor, J. Cao, A.P. Karafillis, M.C. Boyce, Numerical simulations of sheet-metal forming, J. Mater. Process. Technol. 50 (1995) 168–179.
[12] G. Pietrzak, A. Curnier, Large deformation frictional contact mechanics: continuum formulation and augmented Lagrangian treatment, Comput. Methods Appl. Mech. Eng. 177 (1999) 351–381.
[13] D.J. Benson, J.O. Hallquist, A single surface contact algorithm for the post-buckling analysis of shell structures, Comput. Methods Appl. Mech. Eng. 78 (1990) 141–163.
[14] K.J. Bathe, A.B. Chaudhary, A solution method for planar and axisymmetric contact problems, Int. J. Numer. Methods Eng. 21 (1985) 65–88.
[15] J.-H. Heegaard, A. Curnier, An augmented Lagrange method for discrete large slip contact problems, Int. J. Numer. Methods Eng. 36 (1993) 569–593.
[16] P. Wriggers, Finite element algorithms for contact problems, Arch. Comput. Methods Eng. 2 (1995) 1–49.
[17] A. Batailly, B. Magnain, N. Chevaugeon, A comparative study between two smoothing strategies for the simulation of contact with large sliding, Comput. Mech. 51 (2013) 581–601.
[18] M.A. Puso, T.A. Laursen, A 3D contact smoothing method using Gregory patches, Int. J. Numer. Methods Eng. 54 (2002) 1161–1194.
[19] G. Zavarise, L. De Lorenzis, The node-to-segment algorithm for 2D frictionless contact: classical formulation and special cases, Comput. Methods Appl. Mech. Eng. 198 (2009) 3428–3451.
[20] M.A. Puso, T.A. Laursen, A mortar segment-to-segment frictional contact method for large deformations, Comput. Methods Appl. Mech. Eng. 93 (2004) 4891–4913.
[21] B. Yang, T.A. Laursen, X. Meng, Two-dimensional mortar contact methods for large deformation frictional sliding, Int. J. Numer. Methods Eng. 62 (2005) 1183–1225.
[22] B. Yang, T. Laursen, A large deformation mortar formulation of self contact with finite sliding, Comput. Methods Appl. Mech. Eng. 197 (2008) 756–772.
[23] M. Tur, E. Giner, F.J. Fuenmayor, P. Wriggers, 2D contact smooth formulation based on the mortar method, Comput. Methods Appl. Mech. Eng. 247–248 (2012) 1–14.
[24] T. Hama, T. Nagata, C. Teodosiu, A. Makinouchi, H. Takuda, Finite-element simulation of springback in sheet metal forming using local interpolation for tool surfaces, Int. J. Mech. Sci. 50 (2008) 175–192.

[25] N. El-Abbasi, S.A. Meguid, A. Czekanski, On the modelling of smooth contact surfaces using cubic splines, Int. J. Numer. Methods Eng. 50 (2001) 953–967.
[26] L. Krstulovic-Opara, P. Wriggers, J. Korelc, A C^1-continuous formulation for 3D finite deformation friction contact, Comput. Mech. 29 (2002) 27–42.
[27] M. Stadler, G.A. Holzapfel, J. Korelc, C^n continuous modeling of smooth contact surfaces using NURBS and application to 2D problems, Int. J. Numer. Methods Eng. 57 (2003) 2177–2203.
[28] P. Wriggers, L. Krstulovic-Opara, J. Korelc, Smooth C^1-interpolations for two dimensional frictional contact problems, Int. J. Numer. Methods Eng. 51 (2001) 1469–1495.
[29] M. Al-Dojayli, S.A. Meguid, Accurate modeling of contact using cubic splines, Finite Elem. Anal. Des. 38 (2002) 337–352.
[30] V. Padmanabhan, T.A. Laursen, A framework for development of surface smoothing procedures in large deformation frictional contact analysis, Finite Elem. Anal. Des. 37 (2001) 173–198.
[31] M. Stadler, G.A. Holzapfel, Subdivision schemes for smooth contact surfaces of arbitrary mesh topology in 3D, Int. J. Numer. Methods Eng. 60 (2004) 1161–1195.
[32] A. Santos, A. Makinouchi, Contact strategies to deal with different tool descriptions in static explicit FEM of 3-D sheet metal forming simulation, J. Mater. Process. Technol. 50 (1995) 277–291.
[33] A.E. Tekkaya, State-of-the-art of simulation of sheet metal forming, J. Mater. Process. Technol. 103 (2000) 14–22.
[34] A. Heege, P. Alart, A frictional contact element for strongly curved contact problems, Int. J. Numer. Methods Eng. 39 (1996) 165–184.
[35] H.B. Shim, E.K. Suh, Contact treatment algorithm for the trimmed NURBS surface, J. Mater. Process. Technol. 104 (2000) 200–206.
[36] S. Wang, E. Nakamachi, The inside-outside contact search algorithm for finite element analysis, Int. J. Numer. Methods Eng. 40 (1997) 3665–3685.
[37] T. Nagata, Simple local interpolation of surfaces using normal vectors, Comput. Aided Geom. Des. 22 (2005) 327–347.
[38] D.M. Neto, M.C. Oliveira, L.F. Menezes, J.L. Alves, Improving Nagata patch interpolation applied for tool surface description in sheet metal forming simulation, Comput. Aided Des. 45 (2013) 639–656.
[39] L.F. Menezes, C. Teodosiu, Three-dimensional numerical simulation of the deep-drawing process using solid finite elements, J. Mater. Process. Technol. 97 (2000) 100–106.
[40] M.C. Oliveira, J.L. Alves, L.F. Menezes, Algorithms and strategies for treatment of large deformation frictional contact in the numerical simulation of deep drawing process, Arch. Comput. Methods Eng. 15 (2008) 113–162.
[41] Y. Yamada, N. Yoshimura, Plastic stress–strain matrix and its application for the solution of elastic–plastic problems by the finite element method, Int. J. Mech. Sci. 10 (1968) 343–354.
[42] M.C. Oliveira, L.F. Menezes, Automatic correction of the time step in implicit simulations of the stamping process, Finite Elem. Anal. Des. 40 (2004) 1995–2010.
[43] L.F. Menezes, D.M. Neto, M.C. Oliveira, J.L. Alves, Improving computational performance through HPC techniques: case study using DD3IMP in-house code, AIP Conf. Proc. 1353 (2011) 1220–1225.
[44] T.A. Laursen, The convected description in large deformation frictional contact problems, Int. J. Solids Struct. 31 (1994) 669–681.
[45] A. Konyukhov, K. Schweizerhof, Covariant description for frictional contact problems, Comput. Mech. 35 (2005) 190–213.
[46] A.R. Mijar, J.S. Arora, Review of formulations for elastostatic frictional contact problems, Struct. Multi. Optim. 20 (2000) 167–189.
[47] Y. Renard, Generalized Newton's methods for the approximation and resolution of frictional contact problems in elasticity, Comput. Methods Appl. Mech. Eng. 256 (2013) 38–55.
[48] M.C. Oliveira, J.L. Alves, L.F. Menezes, Improvement of a frictional contact algorithm for strongly curved contact problems, Int. J. Numer. Methods Eng. 58 (2003) 2083–2101.
[49] K.J. Bathe, Finite Element Procedures in Engineering Analysis, Prentice-Hall, 1982.
[50] S. Morita, Y. Nishidate, T. Nagata, Y. Yamagata, C. Teodosiu, Ray-tracing simulation method using piecewise quadratic interpolant for aspheric optical systems, Appl. Opt. 49 (2010) 3442–3451.
[51] N. Mendes, P. Neto, J.N. Pires, A. Loureiro, Discretization and fitting of nominal data for autonomous robots, Exp. Syst. Appl. 40 (2013) 1143–1151.
[52] M. Hachani, L. Fourment, A 3D contact smoothing method based on quasi-C^1 interpolation and normal voting – application to 3D forging and rolling, AIP Conf. Proc. 1252 (2010) 487–495.
[53] R.T. Farouki, Closing the gap between CAD model and downstream application, SIAM News 32 (1999) 303–319.
[54] S. Katz, T.W. Sederberg, Genus of the intersection curve of two rational surface patches, Comput. Aided Geom. Des. 5 (1988) 253–258.
[55] D.M. Neto, M.C. Oliveira, L.F. Menezes, J.L. Alves, Nagata patch interpolation using surface normal vectors evaluated from the IGES file, Finite Elem. Anal. Des. 72 (2013) 35–46.
[56] D.M. Neto, M.C. Oliveira, J.L. Alves, L.F. Menezes, Local interpolation for tools surface description, AIP Conf. Proc. 1252 (2010) 479–486.
[57] C. Boschiroli, L. Fünfzig, G. Romani, Albrecht, A comparison of local parametric C^0 Bézier interpolants for triangular meshes, Comput. Graph. UK 35 (2011) 20–34.
[58] Z.H. Zhong, L. Nilsson, A contact searching algorithm for general contact problems, Comput. Struct. 33 (1989) 197–209.
[59] T. Belytschko, M.O. Neal, Contact-impact by the pinball algorithm with penalty and Lagrangian methods, Int. J. Numer. Methods Eng. 31 (1991) 547–572.
[60] M. Oldenburg, L. Nilsson, The position code algorithm for contact searching, Int. J. Numer. Methods Eng. 37 (1994) 359–386.
[61] A. Konyukhov, K. Schweizerhof, On the solvability of closest point projection procedures in contact analysis: analysis and solution strategy for surfaces of arbitrary geometry, Comput. Methods Appl. Mech. Eng. 197 (2008) 3045–3056.
[62] H.R.M. Santos, Validação e optimização de algoritmos de contacto com atrito aplicados a superfícies Nagata (M.Sc. Thesis), University of Coimbra, Portugal, 2012.
[63] V.A. Yastrebov, G. Cailletaud, F. Feyel, A local contact detection technique for very large contact and self-contact problems: sequential and parallel implementations, in: Trends in Computational Contact Mechanics, LNACM, vol. 58, Springer, 2011, pp. 227–251, http://dx.doi.org/10.1007/978-3-642-22167-5_13.
[64] D.S. Malkus, T.J.R. Hughes, Mixed finite element methods – reduced and selective integration techniques: a unification of concepts, Comput. Methods Appl. Mech. Eng. 15 (1978) 63–81.
[65] T.J.R. Hughes, Generalization of selective integration procedures to anisotropic and nonlinear media, Int. J. Numer. Methods Eng. 15 (1980) 1413–1418.
[66] J. Wu, D. Zhou, Specifications for BM2: underbody cross member panel, AIP Conf. Proc. 778 (2005) 1150–1156.
[67] M.F. Shi, M. Huang, Specification for benchmark materials, AIP Conf. Proc. 778 (2005) 1173–1178.
[68] GiD: The personal pre and postprocessor, International Center for Numerical Methods in Engineering (CIMNE). URL: <www.gidhome.com>.
[69] T. Buranathiti, J. Cao, Benchmark simulation results: automotive underbody cross member (benchmark 2), AIP Conf. Proc. 778 (2005) 1004–1112.
[70] T. Buranathiti, J. Cao, Numisheet 2005 benchmark analysis on forming of an automotive underbody cross member: benchmark 2, AIP Conf. Proc. 778 (2005) 1113–1120.